Biochemical Journal (2017) **474** 4019–4034
https://doi.org/10.1042/BCJ20170651

PORTLAND PRESS

Research Article

Mitochondrial DNA density homeostasis accounts for a threshold effect in a cybrid model of a human mitochondrial disease

Juvid Aryaman[1], Iain G. Johnston[2] and Nick S. Jones[1]

[1]Department of Mathematics, Imperial College London, London, U.K.; [2]School of Biosciences, University of Birmingham, Birmingham, U.K.

Correspondence: Nick S. Jones (nick.jones@imperial.ac.uk) or Iain G. Johnston (i.johnston.1@bham.ac.uk)

OPEN ACCESS

Mitochondrial dysfunction is involved in a wide array of devastating diseases, but the heterogeneity and complexity of the symptoms of these diseases challenges theoretical understanding of their causation. With the explosion of omics data, we have the unprecedented opportunity to gain deep understanding of the biochemical mechanisms of mitochondrial dysfunction. This goal raises the outstanding need to make these complex datasets interpretable. Quantitative modelling allows us to translate such datasets into intuition and suggest rational biomedical treatments. Taking an interdisciplinary approach, we use a recently published large-scale dataset and develop a descriptive and predictive mathematical model of progressive increase in mutant load of the MELAS 3243A>G mtDNA mutation. The experimentally observed behaviour is surprisingly rich, but we find that our simple, biophysically motivated model intuitively accounts for this heterogeneity and yields a wealth of biological predictions. Our findings suggest that cells attempt to maintain wild-type mtDNA density through cell volume reduction, and thus power demand reduction, until a minimum cell volume is reached. Thereafter, cells toggle from demand reduction to supply increase, up-regulating energy production pathways. Our analysis provides further evidence for the physiological significance of mtDNA density and emphasizes the need for performing single-cell volume measurements jointly with mtDNA quantification. We propose novel experiments to verify the hypotheses made here to further develop our understanding of the threshold effect and connect with rational choices for mtDNA disease therapies.

Introduction

Mitochondria are organelles which are present across much of eukaryotic life and are known for their role in the production of ATP, the major energy currency of the cell. In humans, mitochondrial dysfunction is associated with a host of diseases because of the role of mitochondria in metabolism, biosynthesis [1] and energy supply, as well as their importance in cell death signalling [2], implicating them in diseases ranging from neurodegeneration [3] to cancer [4]. Fundamental understanding of these organelles and their dysfunction is, therefore, of far-reaching biomedical importance.

Mitochondria generate ATP by pumping electrons across their inner membrane to generate an electrochemical gradient, which is used by ATP synthase to convert ADP into ATP. The process of electron pumping is known as the electron transport chain (ETC), and this pathway of ATP generation is called oxidative phosphorylation (OXPHOS). Mitochondria also possess their own circular DNA (mtDNA), which are held in multiple copies per cell. In humans, these genomes encode 13 proteins (which encode subunits of complexes I, III and IV of the ETC and ATP synthase), 22 tRNAs and 2 rRNAs. An important class of diseases which affect mitochondria are those which are caused by a mutation in mtDNA. The most common, and most studied, of these is MELAS

Received: 24 August 2017
Revised: 24 October 2017
Accepted: 27 October 2017

Accepted Manuscript online: 27 October 2017
Version of Record published: 24 November 2017

Biochemical Journal (2017) 474 4019–4034
https://doi.org/10.1042/BCJ20170651

(mitochondrial encephalomyopathy, lactic acidosis, and stroke-like episodes) syndrome, which is often associated with a mitochondrial tRNA mutation at position 3243A>G of the mitochondrial genome [5,6]. Its incidence rate shows large regional variability, with a prevalence of 1 : 6000 in Finland [7] to 1 : 424 in Australia [8]. tRNAs affected by the mutation cause amino acid misincorporations during translation and generate defective mitochondrial proteins, inducing defective respiration when mutant load (or heteroplasmy, which is the ratio of the mutant mtDNA copy number to the total mtDNA copy number per cell) is high [9].

A common feature in many diseases associated with mutations of mitochondrial DNA, including MELAS, is the non-linear physiological response of cells and tissues to increasing levels of mtDNA heteroplasmy. In particular, cells appear to be able to withstand high levels of heteroplasmy without showing any significant metabolic or physiological defect. For instance, fibroblasts possessing the MELAS mutation were shown to have unaffected respiratory enzyme activity until mutant load exceeded ∼60% [10]. Also, Chomyn et al. [11] showed that oxygen consumption of cells does not significantly reduce until MELAS heteroplasmy exceeds ∼90%. This observation has been named the threshold effect (reviewed in ref. [12]).

It has been argued that the threshold effect occurs because mitochondria possess spare capacity at the translational, enzymatic and biochemical levels, which are each able to absorb some degree of stress and thus delay the phenotypic response of increasing heteroplasmy, until a particular threshold heteroplasmy is exceeded, which is typically large [12]. Within this picture, each physiological feature (such as enzymatic activity or oxygen consumption) may be expected to display step-like behaviour with respect to increasing heteroplasmy. Asynchrony of thresholds between different features, such as 60% for enzyme activity [10] and 90% for oxygen consumption [11], may be explained by spare capacity at intermediate levels. For example, a biochemical threshold effect could account for asynchrony in oxygen consumption and enzyme activity thresholds, where metabolic fluxes are altered to compensate for fewer functional enzymes and hence prolong an oxygen consumption deficit to higher levels of enzymatic dysfunction [12].

A recent study published by Picard et al. [13] established 143B TK$^-$ cybrid osteosarcoma cell lines containing the MELAS 3243A>G mutation across the full-dose response of mutant load. These cybrid cell lines were generated via the transfer of mtDNAs from a lymphoblastoid cell line, derived from a heteroplasmic 3243A>G patient, into 143B TK$^-$ mtDNA-deficient cells. Although cybrid models such as this have had many non-physiological perturbations made to them, the advantage in using this system is that all cells possess the same nuclear background, and can be generated with heteroplasmies across the full spectrum of mutant load. The authors measured a diverse array of features including RNA expression, protein expression, cell volume, growth rates, mitochondrial morphology and mtDNA content. The sheer diversity of data collected, across multiple levels of heteroplasmy, makes this an important dataset in understanding the threshold effect and mitochondrial dysfunction (despite the fact that the experiment consists of a single biological replicate, albeit with several technical replicates). Under the interpretation of the threshold effect presented above, one might expect a monotonic response to heteroplasmy, as spare capacity is depleted and the cell seeks alternative means of energy provision. However, Picard et al. [13] observed complex multiphasic responses across numerous physiological readouts as heteroplasmy was increased.

The authors of the study identified four distinct transcriptional phases in the gene expression profiles of MELAS 3243A>G cells: 0%, 20–30%, 50–90% and 100% mutant load. They argue that continuous changes in heteroplasmy result in discrete changes in phenotype, because there exist a limited number of states that the nucleus can acquire in response to progressive changes in retrograde signalling [13]. In this work, by considering a distilled subset of the data from ref. [13], and using simple, physically motivated arguments, we attempt to provide a simplified account of this dataset to gain better understanding of the consequences of this mutation and the threshold effect.

Our mathematical model suggests that cells attempt to maintain homeostasis in wild-type mtDNA density at low heteroplasmies, through reduction in cell volume and therefore cellular power demand. We propose the existence of a single critical heteroplasmy, where cells are no longer able to maintain wild-type mtDNA density homeostasis, and toggle from power demand reduction to supply increase. In this regime, energy supply pathways are up-regulated. Our model also identifies an additional bioenergetic transition, in excess of 90% mutant load, as cells become fully homoplasmic. We explore the possibility of reduced transcriptional activity in mutant mtDNAs/mitochondria, limited tRNA diffusivity and a connection between cellular proliferation rate and cell volume, finding all of the above to have explanatory power. We propose new experiments to verify the novel hypotheses made here to drive forward understanding of the threshold effect.

Biochemical Journal (2017) **474** 4019–4034
https://doi.org/10.1042/BCJ20170651

Materials and methods

Data normalization

We considered a core subset of six physiological features from the dataset of ref. [13] for mathematical modelling: mitochondrially encoded ETC mRNA pool size, ETC protein levels, glycolysis mRNA pool size, cell volume, cell proliferation rate (or cell growth rate as termed in ref. [13]) and maximal respiratory capacity. We performed many normalizations to the data, the result of which is shown in Figure 1.

OXPHOS, as well as glycolysis, have multiple different mRNAs participating in their respective pathways. To have some measure of the overall expression level of a pathway ($\bar{E}$), we used the mRNA concentration (in RPMK, reads per kilobase of transcript per million mapped reads), for each gene corresponding to enzymes of the pathway ($e_{i,k}(h)$, for gene i and technical replicate k at heteroplasmy h) and took a normalized sum as follows:

$$\bar{E} = \frac{1}{N}\frac{1}{n_r}\sum_{k=1}^{n_r}\sum_{i=1}^{N}\frac{e_{i,k}(h)}{1/n_r\left[\sum_{l=1}^{n_r} e_{i,l}(h=0)\right]}, \tag{1}$$

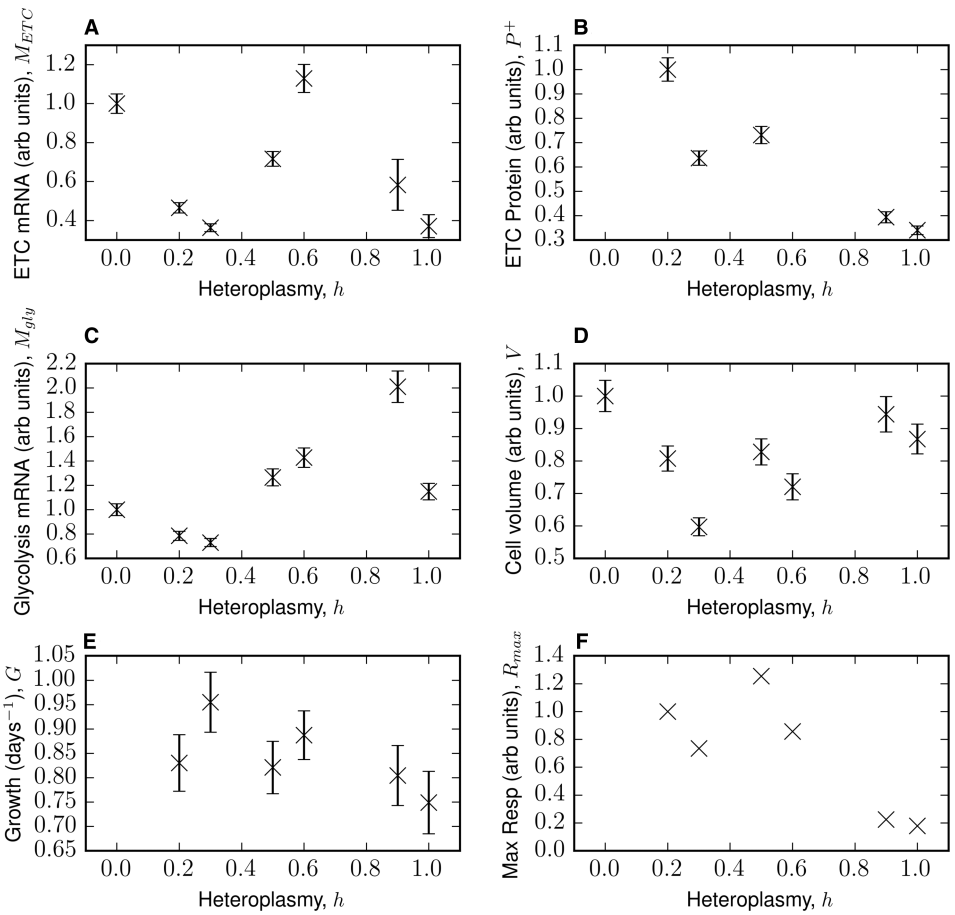

Figure 1. Multiphasic physiological response to increasing heteroplasmy — core data considered from Picard et al. renormalized to be in per-cell dimensions.

Selected measurements of 143B TK$^-$ osteosarcoma cells heteroplasmic in MELAS 3243A>G, from ref. [13]. (**A**) mRNA levels for 11 mitochondrially encoded ETC subunits (COX3, ND2, ND5, CYTB, ND3, ND6, COX1, ND4, COX2, ND1 and ND4L). (**B**) Protein levels for complexes I, III and IV. (**C**) Glycolysis mRNA levels, for genes (PKM2, ENO1, PGAM4, PGK1, GAPDH, ALDOA, PFKP, GPI, HK2 and SLC2A1). All errors in **A–C** are the standard error of the transformed renormalized mean [see eqn (2)]. (**D**) Mean cell volume of an asynchronous population of growing cells ± SEM. (**E**) Growth rate, determined by linear regression. Error is the standard error in the slope from linear regression. (**F**) Maximum respiratory capacity. Details of the data normalization and regression may be found in Materials and Methods. See ref. [13] for experimental protocols.

Biochemical Journal (2017) 474 4019–4034
https://doi.org/10.1042/BCJ20170651

where n_r = number of technical replicates and N = number of genes in the pathway of interest. This quantity normalizes the expression level of each gene to mean $h = 0$ levels, to avoid effects from consistently highly expressed genes. The factor of $1/N$ results in $\bar{E}$ having the value of 1 at $h = 0$, so may be interpreted as a fold-change in expression relative to $h = 0$.

The standard error of $\bar{E}$ over technical replicates k may be written as follows:

$$s_{\bar{E}} = \frac{1}{N}\frac{1}{\sqrt{n_r}}\left(V_k\left[\sum_{i=1}^{N}\frac{e_{i,k}(h)}{1/n_r\left[\sum_{l=1}^{n_r} e_{i,l}(h=0)\right]}\right]\right)^{1/2}, \quad (2)$$

where $V_k(x_k)$ is the sample variance over x_k. Eqns (1) and (2) are applied to glycolysis and ETC mRNAs in our main model, which yield dimensionless, normalized, measures of transcript levels for each biological pathway.

ATP synthase was excluded from both ETC mRNA and protein data, as it is expected to be regulated differently from other ETC proteins. This difference arises because mitochondrial membrane potential is required for cell growth [14], and glycolytic ATP may be used, even in cells without mtDNA, by ATP synthase to maintain membrane potential [15]. Thus, protein levels of ATP synthase may be expected to be regulated quite differently to those of the ETC, and not generally indicative of respiratory activity.

For ETC protein, we simply used the sample mean of complexes I, III and IV, since the data given by Picard et al. [13] are already normalized.

Data transformation to per-cell dimensions

The data we considered of Picard et al. [13] consist of RNA-seq and Western blot measurements for mRNA and protein levels, respectively. We wished to model the bioenergetic strategy of an average cell, so it is important that the data used to parameterize the model are of per-cell dimensions. We show in Supplementary Text S1 that it is appropriate to multiply protein and transcript data by cell volume to gain per-cell dimensions.

Error propagation

Our work focuses on describing the mean behaviour of various cellular processes with respect to heteroplasmy, so uncertainty in these means must be quantified. For M_{gly} and M_{ETC}, we used error propagation on the normalized transcript levels $\bar{E}$ [see eqn (1)] and V, to derive the volume-adjusted transcript uncertainties for the data shown in Figure 1

$$\sqrt{\bar{E}^2 s_V^2 + V^2 s_{\bar{E}}^2} \quad (3)$$

where $s_{\bar{E}}$ is defined in eqn (2) and s_V is the SEM for cell volume (raw data provided by Martin Picard). For the case of ETC protein data, since the corresponding experiments in Picard et al. [13] had only a single technical replicate, we derived an uncertainty by simply multiplying the normalized protein value (see 'Data Normalization') by s_V.

Growth rate determination

The speed with which cells proliferate is dependent on heteroplasmy, as can be seen in Supplementary Figure S1. However, by day 6 of growth, cell growth appeared to change its behaviour, with evidence of saturation; we, therefore, truncated the raw data to day 5 and calculated the exponential growth rate by linear regression in log-lin space.

Model inference

We used Bayesian inference to determine the parametric uncertainty in the mathematical model presented below, given the data in ref. [13], for the six features considered here. We assumed Gaussian noise for the error in the normalized versions of each feature. For full details of the priors used for each feature, see Supplementary Text S2.

Biochemical Journal (2017) **474** 4019–4034
https://doi.org/10.1042/BCJ20170651

Results

Per-cell interpretation of omics data highlights multiphasic dynamics in response to heteroplasmic load

A simple interpretation of the threshold effect predicts the existence of spare capacity in the transcription, translation, enzyme complex and biochemical levels of the cell, in response to increasing heteroplasmy [12]. Under this interpretation of the threshold effect, we might expect all of these functions to have no more than one turning point with increasing heteroplasmy.

However, the data in Figure 1, and indeed the dataset of Picard et al. [13] overall, show a much more complex response. For instance, ETC transcripts clearly show two turning points, suggesting some kind of transient compensatory response. Across the features, these data also appear to be asynchronous in their turning points. For instance, ETC transcripts peak at $h = 0.6$, but glycolysis transcripts peak at $h = 0.9$. This highlights the need for an extension in our understanding of the threshold effect, as well as the challenge in trying to parsimoniously model such a complex dataset.

We note that the measurement uncertainty, reported in [13], for our selected features of interest is small relative to the variation with respect to heteroplasmy (see Figure 1), justifying a non-linear fit to the data. It should be noted, however, that this uncertainty only reflects the technical variability in measurement and does not include potential biological variability of these features. We use a Bayesian approach to appropriately account for this uncertainty (see Supplementary Text S2).

Integrated omics data motivate a model of the causal relationships between bioenergetic variables

We present a qualitative description of our model in Figure 2, which we will develop into a full quantitative description below. One of our central claims is the existence of a single transition in cellular behaviour, in response to increasing heteroplasmy of the 3243A>G mutation, over the 0–90% heteroplasmy range. We propose that, at low heteroplasmy values, *cells attempt to maintain homeostasis in wild-type mtDNA density by reducing their volume*. This reduces biosynthetic and translational power demands, by the simplifying assumption that power demand scales directly with cell volume.

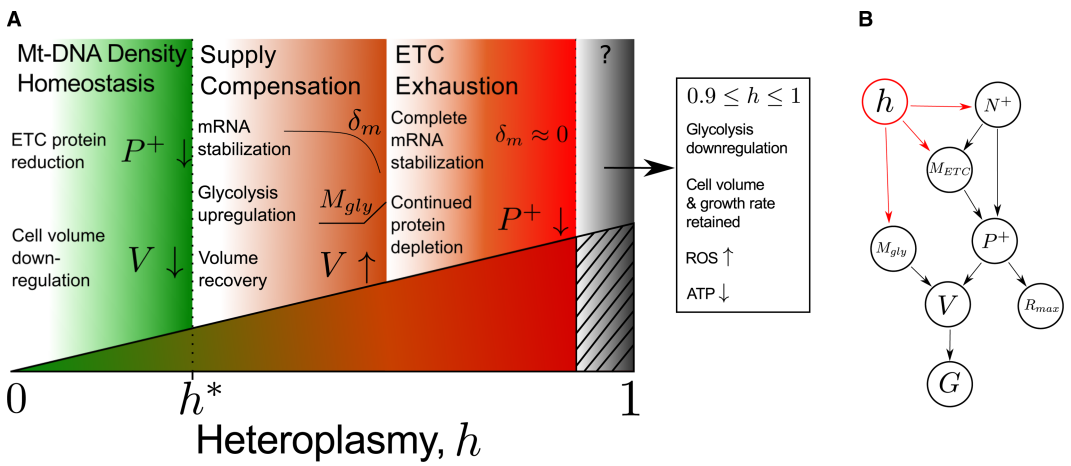

Figure 2. Qualitative description of continuous increase in MELAS mutant load.

(**A**) At low levels of heteroplasmy (h), cells attempt to maintain homeostasis in wild-type mtDNA density by reducing their volume (V). This reduces power demands, allowing power supply/demand balance to be maintained despite rising heteroplasmy. A further increase in heteroplasmy triggers a power demand/supply toggle at a critical heteroplasmy h^*, where energy provision pathways are up-regulated. This includes up-regulation of both oxidative phosphorylation, by reduction in mRNA degradation (δ_m), and glycolysis transcripts (M_{gly}). Cell volume consequently recovers. A further increase in heteroplasmy exhausts ETC stabilization, as $\delta_m \to 0$, and ETC protein (P^+) continues to deplete. In the transition to homoplasmy, glycolysis and ATP levels reduce, yet cell volume and growth rate are retained. In this regime, the mode of energy production is unclear. (**B**) Flow of causality in our mathematical model. N^+, wild-type mtDNA copy number; M_{ETC}, ETC mRNA; R_{max}, maximum respiratory capacity; G, cellular growth rate. Heteroplasmy shown in red connecting to variables with explicit dependence.

Biochemical Journal (2017) 474 4019–4034
https://doi.org/10.1042/BCJ20170651

Our model suggests that at a critical heteroplasmy, h^*, cells undergo a demand/supply toggle where power supply is up-regulated. ETC transcripts are stabilized through reduced degradation, and glycolysis is increased. This bioenergetic compensatory behaviour at intermediate heteroplasmies allows cell volume to recover.

As heteroplasmy continues to increase, we claim that degradation of ETC transcripts becomes negligible. Thus, further increases in heteroplasmy result in reduction in ETC protein content and ETC exhaustion ensues.

These behaviours are captured in the mathematical framework of our model. However, as cells transition from 90 to 100% mutant mtDNA, another transition in cellular behaviour appears to occur, according to the data of ref. [13]. Cells down-regulate glycolysis, yet retain cell volume and growth rate. The mode of energy production in this case is unclear and opens new questions as to the most relevant energy supplies and demands in homoplasmic cells (see 'Key Claims and Predictions of Biophysical Model of Heteroplasmy').

Interactions between bioenergetic variables can be cast as a bottom-up quantitative model

We now present a quantitative description of our model, see Table 1, whose mechanistic interpretations will be more fully explored in the section 'Key Claims and Predictions of Biophysical Model of Heteroplasmy'. Our model attempts to unify the experimentally measured features of ref. [13] within a simple, physically plausible, bottom-up cell biological representation. We stress that our choice of model structure was not developed independently of the data in ref. [13]; hence, at the level of choice of model structure, we have limited control of over-fit. However, the uncertainty in its parameters, given the data and a set of priors (see Supplementary Text S2), was computed using Bayesian inference. So, while our parameterization of the model has statistical control for uncertainty, we have not employed a statistical model selection framework. We believe this to be appropriate and practically unavoidable, as our objective is to yield a new reduced account for these heterogeneous data, present novel hypotheses and propose new experiments.

Wild-type mtDNA scaling

A theme apparent in the data of Picard et al. is an overall downward trend of ETC mRNA and ETC protein with increasing heteroplasmy (h). We, therefore, use the hypothesis that these quantities scale with the amount of wild-type mtDNA (N^+). Total mtDNA copy number showed only a weak dependence on heteroplasmy, with only one heteroplasmy value displaying statistically significant deviation from $h = 0$ copy number (Figure 1I of [13]). We, therefore, assume that N = mtDNA copy number = const (set to 1 after normalization, without loss

Table 1 Mathematical model of MELAS 3243 A>G mutation with progressive mutant load
See Supplementary Table S1 for parameter descriptions. Heteroplasmy = h, mtDNA copy number = N.

Description	Equation	Equation numbers
Wild-type mtDNA, N^+	$N^+ = N(1-h)$	(4)
ETC mRNA, M_{ETC}	$M_{ETC} = \frac{\beta}{\delta_m + 1} N^+$	(5)
	$\delta_m(h) = \frac{k_{mRNA}}{1 + \exp[k_m(h - h_0)]}$	(6)
ETC protein, P^+	$P^+ = \frac{N^+ M_{ETC}}{\delta_p}$	(7)
Glycolysis mRNA, M_{gly}	$M_{gly} = \begin{cases} c_1, & h \le h^* \\ m_2 h + c_2, & h > h^* \end{cases}$	(8)
Cell volume, V	$\underbrace{k_o P^+ + k_g M_{gly}}_{\text{supply}} = \underbrace{V}_{\text{demand}}$	(9)
Growth rate, G	$G = \frac{k_{gr}}{V}$	(10)
Maximum respiratory capacity, R_{max}	$R_{max} = k_p P^+$	(11)

of generality) which then defines N^+, see eqn (4). The successful performance of this simple model for N^+ is shown in Supplementary Figure S2. Note that this model has no free parameters, so was not associated with our inferred posteriors.

ETC mRNA

Transcript copy number is determined by the balance of transcription (β) and degradation (δ_m) rates. Given our assumption of N^+ scaling, it can be shown (see Supplementary Text S3) that eqn (5) may be used to model the ETC mRNA pool size (M_{ETC}). We further assume a constant mean transcription rate β for parsimony and allow the degradation rate δ_m to vary with heteroplasmy in response to cellular signals. We require the degradation rate to be high for low heteroplasmies, and low at high heteroplasmies, to describe the ability of cells to up-regulate their transcript copy number with rising heteroplasmy. A biologically motivated choice of function which achieves this is a sigmoid, see eqn (6), where k_{mRNA}, k_m and h_0 are constants.

ETC protein

It is intuitive to assume that mean protein levels scale with transcript levels, although this relationship may be noisy [16]. Following a similar assumption for ETC mRNA, we also assume that ETC protein (P^+) scales with wild-type mtDNA levels. Using analogous arguments to M_{ETC} (see Supplementary Text S3), we show that a reasonable model for ETC protein is eqn (7), where $\delta_p = \text{const}$, denoting the baseline degradation of mitochondrial protein.

Glycolysis mRNA

We assume that the glycolysis mRNA pool size (M_{gly}) is invariant to heteroplasmy, until a critical heteroplasmy $h^\star$, where glycolysis is gradually up-regulated as a result of cellular control. It is, therefore, parsimonious to assume that glycolysis regulation obeys a spline of a constant and linear model which toggles at $h^\star$, see eqn (8), where c_1 and m_2 are free parameters, and $c_2 = c_1 - m_2 h^\star$, by continuity.

Cell volume

We propose that the power demands of the cell may be well approximated as scaling with cell volume (see Supplementary Text S3 for further discussion). As glycolysis and OXPHOS provide power supply to a first approximation, we assume that mean cell volume in an asynchronous population of cells (V) is effectively determined by a scaled sum of glycolysis and OXPHOS contributions, such that the cell obeys a power supply = power demand relationship, see eqn (9), where k_o, $k_g = \text{const}$. We propose that changes in cellular volume are a long-term adaptation to heteroplasmy and therefore power availability.

From Figure 1, it is clear that this assumption fails at $h = 1$, where glycolysis levels and cell volume are comparable to $h = 0$ levels, and yet ETC proteins are only 30% of wild-type levels. As ATP levels are below wild-type levels in these cells (see Supplementary Figure S6E in [13]), the mode of energy production is not clear and further metabolomic data may be required. We, therefore, exclude all $h = 1$ data and limit the domain of our model to $0 \leq h \leq 0.9$.

Growth rate

We observe that the cellular proliferation rate (which we call growth rate, G, for consistency with ref. [13]) varies with heteroplasmy (see Figure 1). We hypothesize that there exists a relationship between mean cell volume and growth rate. It can be shown that, assuming individual cells increase their volume linearly through the cell cycle, growth rate varies inversely with mean cell volume (shown in Supplementary Text S3). This is shown in eqn (10), where k_{gr} is a constant.

We show in Supplementary Text S3 that, under an exactly exponential model of cell growth, G is independent of V. However, given that there is presumably a wide class of cytoplasmic growth-vs.-time profiles which cells may obey, we use a linear model as a parsimonious example of how cell growth may be connected to cytoplasmic volume.

Maximum respiratory capacity

It has long been recognized that cells carrying the MELAS mutation experience a respiratory defect when heteroplasmic load exceeds ~90% [11,17], and that this is due to a defect in protein synthesis [9,11]. We,

Biochemical Journal (2017) 474 4019–4034
https://doi.org/10.1042/BCJ20170651

therefore, assume that maximum respiratory capacity (R_{max}) is always determined by protein content. This yields a simple linear expression, see eqn (11), where $k_p = \text{const}$.

Model summary

In summary, our model of mean cellular behaviour with respect to heteroplasmy describes seven features from Picard et al. [13] (N^+, M_{ETC}, P^+, M_{gly}, V, G and R_{max}) and has 12 adjustable parameters (as discussed later, this is fewer than the number required for seven linear models with offsets), a table of which is shown in Supplementary Table S1. In writing down this phenomenological model, we have attempted to account for a physiologically important subset of the data generated in ref. [13], using bottom-up arguments wherever possible. In doing so, many novel, falsifiable, hypotheses are made.

Parameterizations of a simple biophysical model account for complex observations across range of heteroplasmic load

The fit of the model described above is shown in Figure 3. Between $0 \leq h \leq h^\star$, $h^\star$ being the critical heteroplasmy where glycolysis is up-regulated ($0.34 \leq h^\star \leq 0.44$, 25–75% CI), our model reproduces the reduction in ETC transcript pool size. Similarly, we observe that ETC protein pool size also reduces, as does cell volume and maximum respiratory capacity.

Our model successfully captures the transient compensatory responses in ETC mRNA, ETC protein and cell volume which begin around the critical heteroplasmy $h^\star$. For heteroplasmies between $h^* \lesssim h \lesssim 0.5$, ETC mRNA degradation reduces causing ETC mRNA to be up-regulated, along with ETC protein and maximum respiratory capacity. In this region, glycolysis becomes induced above wild-type levels, and cell volume can be observed to also recover.

In excess of $h \approx 0.5$, our model shows the observed reductions in ETC mRNA, ETC protein and maximum respiratory capacity. We see that continued up-regulation of glycolysis mRNA allows cell volume to remain at an approximately constant value, although diminished relative to a wild-type cell. Consequently, heteroplasmic cells between $0.2 \leq h \leq 0.9$ are predicted to proliferate at a faster rate than wild-type cells (see Figure 3E).

Key claims and predictions of biophysical model of heteroplasmy

Here, we discuss the interpretations of our model in light of the mathematical description developed above and explore the evidence for the biological insights it provides. We make experimental proposals to validate our claims, which are given in Supplementary Text S4. The set of mechanistic interpretations which follow from our mathematical model are as follows:

- Wild-type mtDNA density is maintained homeostatically at low heteroplasmy.
- There exists a minimum possible cell volume which is approached at the critical heteroplasmy.
- Cells toggle from demand reduction (i.e. cell volume reduction) to supply increase (i.e. glycolysis and ETC mRNA up-regulation), at the critical heteroplasmy.
- Mutant mtDNAs do not significantly contribute to the mitochondrial mRNA pool.
- Mitochondrial tRNAs remain moderately localized to their parent mtDNA.
- Maximum respiratory capacity is determined by ETC protein levels through a linear relationship.
- Cell growth rate is the reciprocal of mean volume, thus smaller cells proliferate faster.

Wild-type mtDNA density homeostasis is maintained until a minimum volume is reached near the critical heteroplasmy

The parameter $h^\star$ determines the extent of mutant load, for which the cell begins to up-regulate ETC mRNA and glycolysis mRNA. But what causes this change in behaviour, at this particular value of heteroplasmy? By examining the posteriors of our model fit (Figure 3), we infer that cell volume takes its minimum value shortly before the most probable value of $h^\star$ (see Figure 4). We hypothesize that an attempt to conserve wild-type mtDNA density (N^+/V) determines the position of $h^\star$.

For $h \lesssim h^*$, wild-type mtDNA density is maintained despite increasing heteroplasmy, because cell volume diminishes. As a result of this reduced demand, the cell can tolerate diminished mitochondrial power supply. However, cell shrinkage cannot continue indefinitely and we hypothesize that the cell reaches a minimum cell volume at $h \approx h^\star$. Once heteroplasmy exceeds this value, the cell toggles its energy balance strategy from power

Biochemical Journal (2017) **474** 4019–4034
https://doi.org/10.1042/BCJ20170651

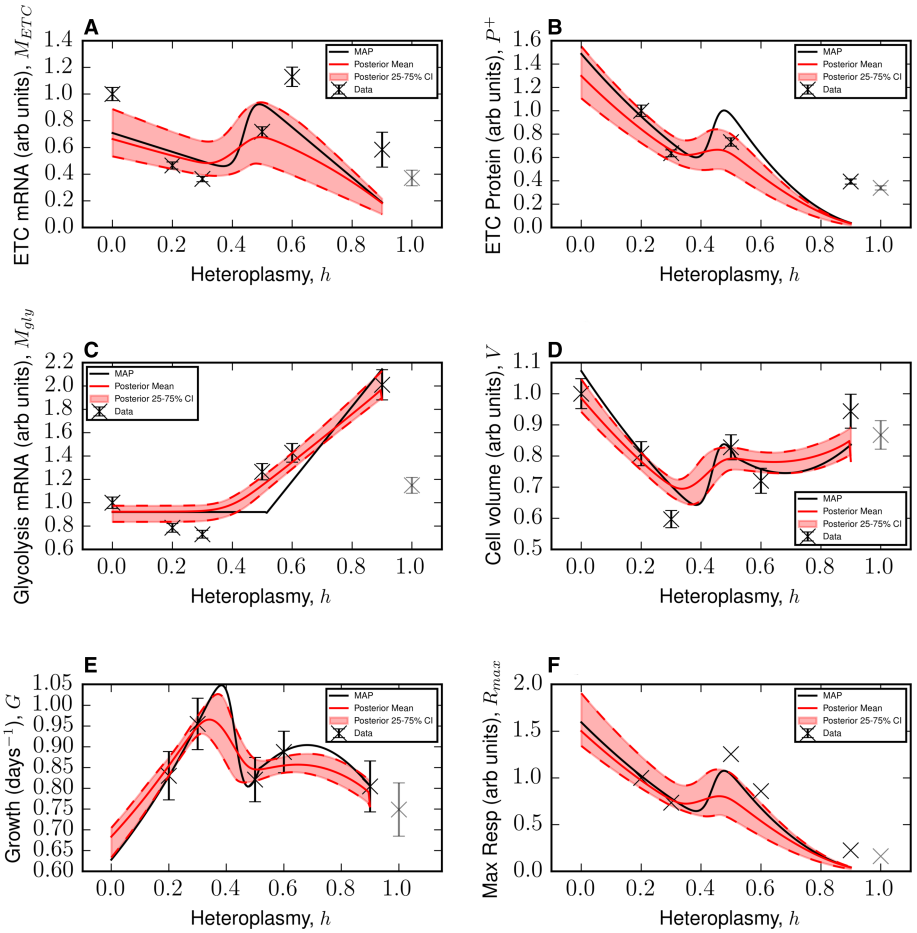

Figure 3. A simple biophysical model is consistent with complex observations across a range of heteroplasmic load.
(**A–F**) Approximations for the maximum a posteriori estimate (black line), posterior mean (red line) and 25–75% Bayesian credible intervals (pink bands), for the model fits to selected data from ref. [13]. The model makes predictions over the range $0 \leq h \leq 0.9$ (see the Main Text). Data for $h = 1$ have been plotted in grey, as they have not been used to train the model. Error bars are conservative and merely show the technical variability reported in ref. [13] (see Materials and Methods).

demand reduction to supply increase, and the cell recovers in volume. We note that this observation was robust to removal of $h = 0.6$ data points where present, see Supplementary Figure S3.

There is evidence in the literature that wild-type mtDNA density is an important quantity. Bentlage and Attardi [17] observed that long-term culture of heteroplasmic MELAS cells resulted in an increase in mtDNA copy number, resulting in increased oxygen consumption. While this was often accompanied by a decrease in heteroplasmy, some cell lines also exhibited this at constant heteroplasmy. This is consistent with the cell attempting to increase the absolute number of wild-type mtDNAs, perhaps to compensate for heteroplasmic load, and suggests that the absolute value of N^+ is a physiologically important quantity.

The density of mitochondrial content per unit cytoplasmic volume has been observed by many authors to be tightly regulated and physiologically predictive. The historical observations of Posakony et al. [18] showed that the mean ratio of mitochondrial content to cytoplasmic volume is kept relatively constant throughout the cell cycle in HeLa cells, occupying ~10–11% of cytoplasmic area throughout. Similar observations have been reproduced in more recent studies, in various other systems. Rafelski et al. [19] found in budding yeast that mitochondrial content was proportional to bud size, and that all buds attain the same average ratio regardless of the mother's age or mitochondrial content, suggesting a stable scaling relation. Also, Johnston et al. [20] found that the density of mitochondrial mass was predictive of cell cycle dynamics, indicating that N/V ($N =$ total number of mtDNAs) is physiologically relevant and potentially linked to cell power supply and growth dynamics.

Biochemical Journal (2017) **474** 4019–4034
https://doi.org/10.1042/BCJ20170651

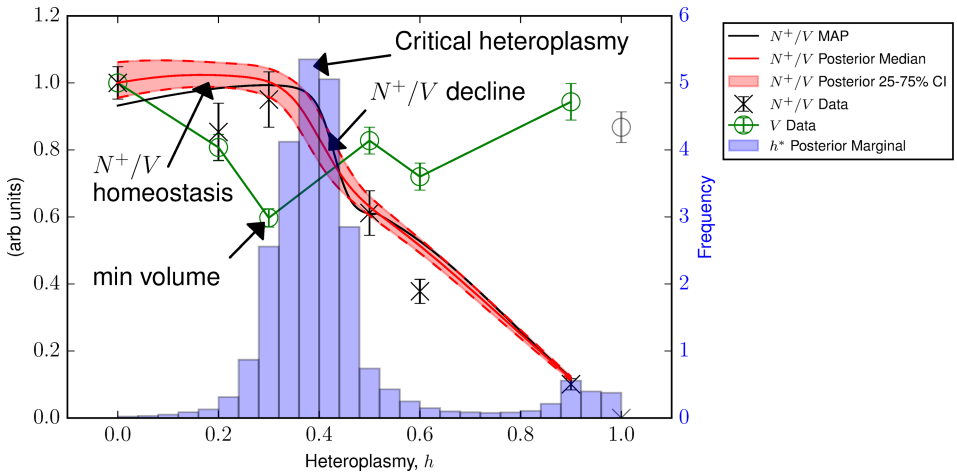

Figure 4. Wild-type mtDNA density (N^+/V) homeostasis may trigger supply/demand toggle.

Posterior statistics show an initial maintenance of N^+/V. When cell volume (V) takes its minimum value, the most probable value of h^* shortly follows. N^+/V then reduces. We suggest that the inability of the cell to maintain $N^+/V = \text{const}$, due to the existence of a minimum cell volume, causes cells to toggle in their strategy at h^*, from demand reduction to supply increase. Data from ref. [13].

Indeed, Jajoo, Paulsson and co-workers [21] found that the density of mitochondrial DNA tracks the quantity of cytoplasm inherited upon division in wild-type fission yeast. Most recently, re-analysis of a work by Miettinen and Björklund [22] found a scaling relationship between cell volume and mitochondrial mass in a population of normal cells [23]: the assumption of constant mitochondrial density was subsequently found to be explanatory in accounting for the data of Miettinen and Björklund [22] using mathematical modelling [23].

We may speculate as to the interpretation of a minimum possible cell volume. One straightforward interpretation is that a minimum cell volume corresponds to a mechanical constraint: a cell may only become so small, because the machinery required to perform tissue-specific metabolic and structural tasks requires a minimum amount of space. Alternatively, a bioenergetic limit to cell volume may exist. For instance, appreciable power demands which scale with, for example, surface area or are invariant to cell size [24–26], may become large relative to power supply as cells become smaller. This is because cellular power supply (through glycolysis and oxidative phosphorylation) likely scales with cell volume. This mismatch in scaling behaviour between power supply and power demand may place a constraint on the minimum cell size.

ETC mRNA degradation diminishes at the critical heteroplasmy contributing to power demand/supply toggle

The induction of glycolysis at the critical heteroplasmy is observed in our model by construction, see eqn (8), since glycolysis is modelled to increase linearly when heteroplasmy exceeds this point. However, by observing the posterior distribution of the ETC mRNA degradation rate (see Figure 5), we see that the critical heteroplasmy also coincides with the beginning of reduction in ETC transcript degradation with respect to heteroplasmy. Since ETC mRNA pool size varies with the inverse of this degradation rate [see eqn (5)], ETC transcripts are consequently up-regulated in tandem with glycolysis transcripts. This occurs until ETC degradation diminishes to negligible levels around $h \approx 0.5$, where this particular control mechanism becomes exhausted. Thus, the critical heteroplasmy coincides with a shift from power demand reduction to supply increase from both glycolysis and OXPHOS contributions.

Since mtDNA is transcribed as a single polycistronic transcript [27], the relative stoichiometry of individual mRNA species must be controlled via active degradation. This is achieved by a balance between processes which stabilize and degrade mRNA [28]. The Picard dataset can be explored further to seek corroborating evidence, by observing the ratio of ETC mRNA degraders to stabilizers. We find a qualitative similarity between this ratio (see Supplementary Figure S4) and the posterior distribution of the ETC degradation rate (see Figure 5), both displaying a substantial reduction between $h = 0.3$ and $h = 0.5$.

Biochemical Journal (2017) **474** 4019–4034
https://doi.org/10.1042/BCJ20170651

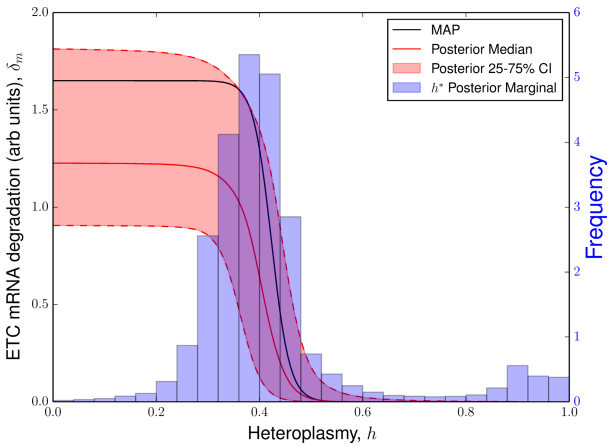

Figure 5. Critical heteroplasmy induces ETC mRNA stabilization.

Posterior distributions for ETC mRNA degradation rate and critical heteroplasmy ($0.34 \leq h^* \leq 0.44$, 25–75% CI and $0.27 \leq h^* \leq 0.89$, 5–95% CI). It can be seen that the critical heteroplasmy coincides with the reduction in ETC degradation, signalling a power demand/supply toggle.

Mitochondrial tRNAs are enriched in the vicinity of their corresponding parental mtDNA

The co-location for redox regulation (CoRR) hypothesis states that mtDNA exists in the close proximity of respiratory units for the rapid and direct regulatory control of respiration [29,30]. This hypothesis, which aligns with several leading theories on the origins of complex life [31,32], has recently been supported by studying mitochondrial gene loss throughout the eukaryotic tree of life [33], as well as other experimental evidence reviewed in ref. [30].

Given the CoRR hypothesis, one might expect there to exist a functional link between the genotype of an mtDNA and the phenotype of its spatially closest respiratory units. In other words, mitochondrial nucleoids (protein–DNA complexes which are thought to possess ∼1.1 mtDNA molecules per nucleoid [34]) may each have a limited sphere of influence; this has been put forward as the 'leaky-link' hypothesis by other authors [35,36].

The 3243A>G MELAS mutation causes amino acid misincorporations, resulting in unstable translation products [9]. It is reasonable to assume that mutant mtDNAs have a locally higher concentration of mutant tRNAs, since they are the source of these molecules, as well as the presence of cristae which may limit diffusion in the mitochondrial matrix [37]. ETC mRNAs in the vicinity of mutant mtDNAs will more often be translated into unstable protein due to the presence of defective tRNAs. Therefore, mutant mtDNAs may give a weaker contribution to the total functional ETC protein content of the cell than wild-type mtDNAs. Hence, low diffusivity inside the mitochondrial matrix is hypothesized to induce a local phenotype–genotype link [35,36]. We take the limit of mutant mtDNAs providing zero contribution to the total ETC protein content of the cell, rather than a limited contribution, for parsimony — i.e. $P^+ \propto M_{\mathrm{ETC}} N^{+\cdot}$ This is equivalent to assuming a strong local phenotype–genotype link. See Supplementary Text S5 for an alternative model of well-mixed tRNAs.

Evidence in the literature for this claim is mixed. It has been observed that mitochondrial mRNAs localize to mtDNA, suggesting that mtDNA may be a site for mitochondrial translation [38,39]. However, cybrid experiments by Ono et al. [40] involving homoplasmic tRNA mutants 3243A>G and 4269A>G are able to recover their respiratory function by fusing such cells together to form hybrids. Their recovery is presumably due to the diffusion of the healthy form of each tRNA, so that normal proteins may be translated. Yet, one might expect there to exist at least limited local coupling between mtDNA and their gene products under the CoRR hypothesis [29,30,33] and the leaky-link hypothesis [35,36], as described above. It is noteworthy that the cybrid experiments by Ono et al. [40] show recovered respiration after a long adaptation phase of 10 days. Since this is a much larger timescale than that of mtDNA replication, which is typically hours [41], it is conceivable that some kind of long-term adaptation occurred in this system which is still compatible with a strong local phenotype–genotype link; for example, the presence of nucleoids with an mtDNA of each kind of mutant, allowing the local transcription of both of the corresponding wild-type tRNAs. See Supplementary Text S4 and Table S2 for experimental suggestions to determine the extent of tRNA diffusivity.

Biochemical Journal (2017) 474 4019–4034
https://doi.org/10.1042/BCJ20170651

Mutant mtDNAs have a transcriptional defect

It has been hypothesized that, due to the limited diffusion of gene products, mutant mtDNAs may experience a local energy deficiency [36]. This local energy deficiency could conceivably reduce the ability of mutant mtDNAs to perform transcription through a local depletion of ATP. Since the concentration of ATP inside the mitochondrial matrix is low in the physiological setting [42], this may leave processes in the vicinity of mutant mtDNAs with increased susceptibility to local fluctuations in energy availability. If mutated mtDNAs are transcribed more slowly, they may have a lower contribution to the ETC transcript pool.

Alternatively, some other mechanism may generate a functional dependence between mitochondrial transcription and mtDNA genotype. For instance, mitochondrial transcription machinery (such as mitochondrial RNA polymerase, POLRMT) could be preferentially transported to functional mtDNAs, potentially via membrane potential sensing. Since dysfunctional mitochondria are observed to bud off from fused networks [43], it is possible that this mechanism allows the cell to sense the individual performance of mitochondria/mtDNAs [44] and hence target nuclear proteins accordingly. It is also possible that mitochondrial translational machinery could be preferentially targeted to functional mitochondria, which would also result in $P^+ \sim N^+$.

We adopted a model of no transcription for mutant mtDNAs, as opposed to limited transcription, for parsimony — i.e. $M_{\mathrm{ETC}} \sim N^+$. See Supplementary Text S5 for an alternative model where mutant mtDNAs provide a non-zero contribution to M_{ETC}. We provide experimental suggestions for determining the extent of mutant mtDNA transcription in Supplementary Text S4.

Cell volume is not explained by cell cycle variations

Our model predicts that cells, on average, change their size as heteroplasmy is varied, due to variation in power supply from OXPHOS and glycolysis. However, since cells vary their volume by a factor of 2 throughout the cell cycle, it is possible that cells with different heteroplasmies spend different durations at various stages of the cell cycle, explaining the observed variation in expected cell volume with heteroplasmy (see Figure 1D). We sought evidence for this hypothesis by computing the ratio of the expression level for genes associated with different stages of the cell cycle [45] (see Supplementary Figure S5). However, we found little evidence to support the enrichment of cell cycle markers at any particular level of heteroplasmy.

OXPHOS contributions to power supply are stabilized at the critical heteroplasmy

The relative contribution of OXPHOS to power supply, i.e. $k_{\mathrm{o}}P^+/(k_{\mathrm{o}}P^+ + k_{\mathrm{g}}M_{\mathrm{gly}})$, is also interesting to observe as heteroplasmy is varied. We observed a transient stabilization in OXPHOS contributions around h^*. A discussion of this is presented in Supplementary Text S6.

Cells proliferate inversely with their size

Owing to our reciprocal model connecting cell volume and growth [see eqn (10)], our model suggests that wild-type cells proliferate more slowly relative to heteroplasmic cells due to their larger size.

Maximum respiratory capacity linearly tracks ETC protein content

It has long been suggested that cells above a particular threshold heteroplasmy experience a respiratory defect [10,11,17]. With a more classical interpretation of the threshold effect, we might have expected the need for a model which has switching behaviour in excess of 60% heteroplasmy [10] for maximum respiratory capacity, in analogy with glycolysis transcript levels [see eqn (8)]. However, in our model, we found that a simple linear relationship between ETC protein and maximum respiratory capacity was sufficient to describe the data available [see eqn (11)].

Reactive oxygen species may explain the transition to homoplasmy, but the corresponding mode of energy production remains unclear

In eqn (9), we claim that cell volume is determined by the weighted sum of glycolysis transcripts and ETC protein. Over the range $0.9 < h \leq 1$, glycolysis transcripts reduce by 57%, whereas ETC protein and cell volume remain comparable, thus breaking the supply = demand relationship, as we have modelled it. Consequently, our model fails to describe the transition from $h = 0.9 \rightarrow 1$.

A potential explanation for the reduction in glycolysis transcripts over this range comes from the fact that glycolysis provides substrate for oxidative phosphorylation. Damaged ETC proteins may produce an excess of

reactive oxygen species (ROS) [46], which can damage mitochondrial proteins, DNA and membranes. If, at high heteroplasmy, any flux through the ETC causes high levels of ROS, then cells may attempt to reduce flux through glycolysis, to avoid production of these species.

Some evidence from Picard et al. supports this hypothesis, where superoxide dismutase (SOD) activity is largely constant with heteroplasmy, except for homoplasmic mutant MELAS cells, which have ∼20% higher SOD activity than wild-type cells (see Supplementary Figure S7D of [13]). Furthermore, it is known that ROS can reversibly inhibit the activity of GAPDH, one of the enzymes involved in glycolysis [47,48].

However, given that fatty acid oxidation (see Supplementary Figure S6) is strongly down-regulated over this range, it remains unexplained how homoplasmic mutant cells maintain their cell volume (and growth rate), given their reduced reliance upon mitochondrial and glycolytic metabolism. Further metabolomic measurements may be required to uncover this mode of energy production.

ATP levels are also observed to decrease over this range (see Supplementary Figure S6E of [13]), which may even suggest that an alternative fuel currency besides ATP supports the growth and size of these cells. However, more careful investigation of this observation may be of value, since it is important to draw the distinction between ATP pool sizes and ATP fluxes, the latter perhaps being more indicative of ATP usage, and the former being indicative of only relative production/consumption rates.

Discussion

In the present study, through the use of a distilled subset of data from ref. [13] and using minimal arguments, we have attempted to explore the apparent marked difference between the complex multiphasic observations of Picard et al. and the classical step-like models associated with the threshold effect.

We note that the model presented here relies on data from cybrid cells [13]. Such cell lines are often unstable in the number of chromosomes that they possess, and the cybridization process itself may induce transcriptional [49] and metabolic changes [50]. A technical concern one may raise with the dataset of Picard et al. [13] is, therefore, the extent to which their observations may be explained by random genetic drift in the nucleus. However, Picard et al. [13] point out that the observations made with respect to heteroplasmy (at least for a subset of features) appear to be non-random with respect to increasing heteroplasmy: for example, the expression of heat shock proteins appeared to increase monotonically with heteroplasmy, which would not be expected under unbiased random perturbations at each level of heteroplasmy. We note also that cybrid systems are not without merit, as cells have the same nuclear background (although this background may be volatile), and have furthered progress in understanding mitochondrial dysfunction (reviewed in ref. [51]). As is the case generally with model biological systems, it is important to seek corroborating evidence from multiple model systems before accepting the observations from any single experiment. Hence, we have suggested a range of experiments to validate the hypotheses we have generated here.

We have argued that a single critical heteroplasmy, h^*, is sufficient to explain this subset of data over the heteroplasmy range $0 \leq h \leq 0.9$ and that other multiphasic behaviour arises naturally from the simple physical/biological assumptions of our model. Our model suggests that cells undergo a power demand/supply toggle at h^*, from demand reduction to supply increase. We hypothesize that homeostasis in wild-type mtDNA density is maintained via cell volume reduction, ensuring that the available functioning power sources are matched to a corresponding level of cellular demand, until a minimum cell volume is reached which coincides with h^*. This triggers the demand/supply bioenergetic toggle where energy production pathways are up-regulated. We believe that this re-emphasizes the need for quantification of single-cell mtDNA content to be associated with volume measurements of the same cell: mtDNA density is a relevant physiological variable [18–21,52]. We find that the mode of energy production over the range $0.9 \leq h \leq 1$ is unclear, and that further metabolomic investigations may be required to determine this.

Our model further predicts that mutant mtDNAs have a reduced contribution to transcription and that tRNAs have low diffusivity. These hypotheses potentially follow from the 'leaky-link' hypothesis whereby mtDNAs have a limited extent of influence, such that there exists a phenotype–genotype link between an mtDNA and its spatially closest respiratory units [35,36]. We also predict that a relationship exists between mean cell volume and cell growth.

A potential consequence of our predictions is that modulation of either mtDNA copy number, wild-type mtDNA copy number or wild-type mtDNA copy number density to ensure optimal values of wild-type mtDNA copy number density could be valuable control axes in therapy. Increasing mitochondrial DNA copy number, for instance through activation of the PGC-1α pathway, may facilitate the increase in cell volume,

Biochemical Journal (2017) **474** 4019–4034
https://doi.org/10.1042/BCJ20170651

deferring the critical heteroplasmy to higher values by delaying the approach towards a minimum cell volume. We might reason that this enhances a wild-type phenotype at higher heteroplasmy values, potentially deferring the full MELAS phenotype to higher heteroplasmies, which typically appears between ∼50 and 90% mutant load [53]. Indeed, it has been found that increasing mitochondrial biogenesis can ameliorate mitochondrial myopathy *in vivo* [54].

We might also argue that as cells toggle from power demand reduction to supply increase, further bolstering of this compensatory response may have clinical significance. For instance, since we observe that cells switch to glycolytic metabolism to compensate for diminishing mitochondrial power supply, further encouragement of this energy mode may be therapeutic. This is supported by the recent observation that promoting the hypoxia response is protective against multiple forms of respiratory chain inhibition [55]. Alternatively, since we predict that cells innately down-regulate ETC mRNA degradation, seeking to up-regulate mitochondrial transcription may aid the cell in maintaining a sufficient mRNA pool size. Furthermore, promoting alternative energy production pathways such as fatty acid oxidation via the ketogenic diet may also aid in reducing the dependence on oxidative phosphorylation. This diet has been associated with increased mitochondrial transcripts [56], mitochondrial content [56,57] and has been shown to slow mitochondrial myopathy progression in transgenic Deletor mice [57]. Indeed, the diet has recently been used in clinic as an adjunctive therapy for a patient suffering from MELAS, harbouring the 3260A>G mutation, which successfully decreased the frequency of seizures and stroke-like episodes [58].

Abbreviations

CoRR, co-location for redox regulation; ETC, electron transport chain; MELAS, mitochondrial encephalomyopathy, lactic acidosis and stroke-like episodes; OXPHOS, oxidative phosphorylation; ROS, reactive oxygen species; SOD, superoxide dismutase.

Author Contribution

N.S.J. and I.G.J. devised the project. J.A., I.G.J. and N.S.J. developed the theory. J.A. carried out the analysis and wrote the manuscript with input from I.G.J. and N.S.J.

Funding

J.A. is supported by the Biotechnology and Biological Sciences Research Council [grant code BB/J014575/1]. I.G.J. was supported by a Medical Research Council fellowship [MR/J013617/1] and a Birmingham Fellowship from the University of Birmingham. N.S.J. is supported by Engineering and Physical Sciences Research Council [grant code EP/N014529/1].

Acknowledgements

We are grateful to Martin Picard for providing raw data, advice on our model, and experimental suggestions. Till Hoffmann provided technical advice for the Bayesian inference aspects of our work. We thank David Fell, Thomas Ouldridge, Thomas McGrath and Hanne Hoitzing for their useful comments and suggestions.

Competing Interests

The Authors declare that there are no competing interests associated with the manuscript.

References

1 Ahn, C.S. and Metallo, C.M. (2015) Mitochondria as biosynthetic factories for cancer proliferation. *Cancer Metab.* **3**, 1 https://doi.org/10.1186/s40170-015-0128-2

2 Taylor, R.C., Cullen, S.P. and Martin, S.J. (2008) Apoptosis: controlled demolition at the cellular level. *Nat. Rev. Mol. Cell Biol.* **9**, 231–241 https://doi.org/10.1038/nrm2312

3 Lin, M.T. and Beal, M.F. (2006) Mitochondrial dysfunction and oxidative stress in neurodegenerative diseases. *Nature* **443**, 787–795 https://doi.org/10.1038/nature05292

4 Wallace, D.C. (2012) Mitochondria and cancer. *Nat. Rev. Cancer* **12**, 685–698 https://doi.org/10.1038/nrc3365

5 Elliott, H.R., Samuels, D.C., Eden, J.A., Relton, C.L. and Chinnery, P.F. (2008) Pathogenic mitochondrial DNA mutations are common in the general population. *Am. J. Hum. Genet.* **83**, 254–260 https://doi.org/10.1016/j.ajhg.2008.07.004

6 Newkirk, J.E., Taylor, R.W., Howell, N., Bindoff, L.A., Chinnery, P.F., Alberti, K.G.M.M. et al. (1997) Maternally inherited diabetes and deafness: prevalence in a hospital diabetic population. *Diabetic Med.* **14**, 457–460<457::AID-DIA372>3.0.CO;2-W

7 Majamaa, K., Moilanen, J.S., Uimonen, S., Remes, A.M., Salmela, P.I., Kärppä, M. et al. (1998) Epidemiology of A3243G, the mutation for mitochondrial encephalomyopathy, lactic acidosis, and strokelike episodes: prevalence of the mutation in an adult population. *Am. J. Hum. Genet.* **63**, 447–454 https://doi.org/10.1086/301959
8 Manwaring, N., Jones, M.M., Wang, J.J., Rochtchina, E., Howard, C., Mitchell, P. et al. (2007) Population prevalence of the MELAS A3243G mutation. *Mitochondrion* **7**, 230–233 https://doi.org/10.1016/j.mito.2006.12.004
9 Sasarman, F., Antonicka, H. and Shoubridge, E.A. (2008) The A3243G tRNALeu (UUR) MELAS mutation causes amino acid misincorporation and a combined respiratory chain assembly defect partially suppressed by overexpression of EFTu and EFG2. *Hum. Mol. Genet.* **17**, 3697–3707 https://doi.org/10.1093/hmg/ddn265
10 Miyabayashi, S., Hanamizu, H., Nakamura, R., Endo, H. and Tada, K. (1992) Defects of mitochondrial respiratory enzymes in cloned cells from MELAS fibroblasts. *J. Inherit. Metab. Dis.* **15**, 797–802 https://doi.org/10.1007/BF01800024
11 Chomyn, A., Martinuzzi, A., Yoneda, M., Daga, A., Hurko, O., Johns, D. et al. (1992) MELAS mutation in mtDNA binding site for transcription termination factor causes defects in protein synthesis and in respiration but no change in levels of upstream and downstream mature transcripts. *Proc. Natl Acad. Sci. U.S.A.* **89**, 4221–4225 https://doi.org/10.1073/pnas.89.10.4221
12 Rossignol, R., Faustin, B., Rocher, C., Malgat, M., Mazat, J.-P. and Letellier, T. (2003) Mitochondrial threshold effects. *Biochem. J.* **370**, 751–762 https://doi.org/10.1042/bj20021594
13 Picard, M., Zhang, J., Hancock, S., Derbeneva, O., Golhar, R., Golik, P. et al. (2014) Progressive increase in mtDNA 3243A>G heteroplasmy causes abrupt transcriptional reprogramming. *Proc. Natl Acad. Sci. U.S.A.* **111**, E4033–E4042 https://doi.org/10.1073/pnas.1414028111
14 Martínez-Reyes, I., Diebold, L.P., Kong, H., Schieber, M., Huang, H., Hensley, C.T. et al. (2016) TCA cycle and mitochondrial membrane potential are necessary for diverse biological functions. *Mol. Cell* **61**, 199–209 https://doi.org/10.1016/j.molcel.2015.12.002
15 Appleby, R.D., Porteous, W.K., Hughes, G., James, A.M., Shannon, D., Wei, Y.-H. et al. (1999) Quantitation and origin of the mitochondrial membrane potential in human cells lacking mitochondrial DNA. *Eur. J. Biochem.* **262**, 108–116 https://doi.org/10.1046/j.1432-1327.1999.00350.x
16 Bar-Even, A., Paulsson, J., Maheshri, N., Carmi, M., O'Shea, E., Pilpel, Y. et al. (2006) Noise in protein expression scales with natural protein abundance. *Nat. Genet.* **38**, 636–643 https://doi.org/10.1038/ng1807
17 Bentlage, H.A.C.M. and Attardi, G. (1996) Relationship of genotype to phenotype in fibroblast-derived transmitochondrial cell lines carrying the 3243 mutation associated with the MELAS encephalomyopathy: shift towards mutant genotype and role of mtDNA copy number. *Hum. Mol. Genet.* **5**, 197–205 https://doi.org/10.1093/hmg/5.2.197
18 Posakony, J.W., England, J.M. and Attardi, G. (1977) Mitochondrial growth and division during the cell cycle in HeLa cells. *J. Cell Biol.* **74**, 468–491 https://doi.org/10.1083/jcb.74.2.468
19 Rafelski, S.M., Viana, M.P., Zhang, Y., Chan, Y.-H.M., Thorn, K.S., Yam, P. et al. (2012) Mitochondrial network size scaling in budding yeast. *Science* **338**, 822–824 https://doi.org/10.1126/science.1225720
20 Johnston, I.G., Gaal, B., das Neves, R.P., Enver, T., Iborra, F.J. and Jones, N.S. (2012) Mitochondrial variability as a source of extrinsic cellular noise. *PLoS Comput. Biol.* **8**, e1002416 https://doi.org/10.1371/journal.pcbi.1002416
21 Jajoo, R., Jung, Y., Huh, D., Viana, M.P., Rafelski, S.M., Springer, M. et al. (2016) Accurate concentration control of mitochondria and nucleoids. *Science* **351**, 169–172 https://doi.org/10.1126/science.aaa8714
22 Miettinen, T.P. and Björklund, M. (2016) Cellular allometry of mitochondrial functionality establishes the optimal cell size. *Dev. Cell* **39**, 370–382 https://doi.org/10.1016/j.devcel.2016.09.004
23 Aryaman, J., Hoitzing, H., Burgstaller, J.P., Johnston, I.G. and Jones, N.S. (2017) Mitochondrial heterogeneity, metabolic scaling and cell death. *BioEssays* **39**, 1700001 https://doi.org/10.1002/bies.201700001
24 Buttgereit, F., Brand, M.D. and Müller, M. (1992) Cona induced changes in energy metabolism of rat thymocytes. *Biosci. Rep.* **12**, 109–114 https://doi.org/10.1007/BF02351215
25 Brand, M.D., Couture, P., Else, P.L., Withers, K.W. and Hulbert, A.J. (1991) Evolution of energy metabolism. Proton permeability of the inner membrane of liver mitochondria is greater in a mammal than in a reptile. *Biochem. J.* **275**, 81–86 https://doi.org/10.1042/bj2750081
26 Rolfe, D.F. and Brown, G.C. (1997) Cellular energy utilization and molecular origin of standard metabolic rate in mammals. *Physiol. Rev.* **77**, 731–758 PMID:9234964
27 Ojala, D., Montoya, J. and Attardi, G. (1981) tRNA punctuation model of RNA processing in human mitochondria. *Nature* **290**, 470–474 https://doi.org/10.1038/290470a0
28 Chujo, T., Ohira, T., Sakaguchi, Y., Goshima, N., Nomura, N., Nagao, A. et al. (2012) LRPPRC/SLIRP suppresses PNPase-mediated mRNA decay and promotes polyadenylation in human mitochondria. *Nucleic Acids Res.* **40**, 8033–8047 https://doi.org/10.1093/nar/gks506
29 Allen, J.F. (1993) Control of gene expression by redox potential and the requirement for chloroplast and mitochondrial genomes. *J. Theor. Biol.* **165**, 609–631 https://doi.org/10.1006/jtbi.1993.1210
30 Allen, J.F. (2003) The function of genomes in bioenergetic organelles. *Philos. Trans. R. Soc. Lond. B Biol. Sci.* **358**, 19–38 https://doi.org/10.1098/rstb.2002.1191
31 Lane, N. and Martin, W. (2010) The energetics of genome complexity. *Nature* **467**, 929–934 https://doi.org/10.1038/nature09486
32 Lane, N. (2011) Energetics and genetics across the prokaryote-eukaryote divide. *Biol. Direct* **6**, 35 https://doi.org/10.1186/1745-6150-6-35
33 Johnston, I.G. and Williams, B.P. (2016) Evolutionary inference across eukaryotes identifies specific pressures favoring mitochondrial gene retention. *Cell Syst.* **2**, 101–111 https://doi.org/10.1016/j.cels.2016.01.013
34 Kukat, C., Davies, K.M., Wurm, C.A., Spåhr, H., Bonekamp, N.A., Kühl, I. et al. (2015) Cross-strand binding of TFAM to a single mtDNA molecule forms the mitochondrial nucleoid. *Proc. Natl Acad. Sci. U.S.A.* **112**, 11288–11293 https://doi.org/10.1073/pnas.1512131112
35 Kowald, A. and Kirkwood, T.B.L. (2011) Evolution of the mitochondrial fusion-fission cycle and its role in aging. *Proc. Natl Acad. Sci. U.S.A.* **108**, 10237–10242 https://doi.org/10.1073/pnas.1101604108
36 Busch, K.B., Kowald, A. and Spelbrink, J.N. (2014) Quality matters: how does mitochondrial network dynamics and quality control impact on mtDNA integrity? *Philos. Trans. R. Soc. B Biol. Sci.* **369**, 20130442 https://doi.org/10.1098/rstb.2013.0442
37 Dieteren, C.E.J., Gielen, S.C.A.M., Nijtmans, L.G.J., Smeitink, J.A.M., Swarts, H.G., Brock, R. et al. (2011) Solute diffusion is hindered in the mitochondrial matrix. *Proc. Natl Acad. Sci. U.S.A.* **108**, 8657–8662 https://doi.org/10.1073/pnas.1017581108

Biochemical Journal (2017) **474** 4019–4034
https://doi.org/10.1042/BCJ20170651

38 Iborra, F.J., Kimura, H. and Cook, P.R. (2004) The functional organization of mitochondrial genomes in human cells. *BMC Biol.* **2**, 9 https://doi.org/10.1186/1741-7007-2-9

39 Ozawa, T., Natori, Y., Sato, M. and Umezawa, Y. (2007) Imaging dynamics of endogenous mitochondrial RNA in single living cells. *Nat. Methods* **4**, 413–419 https://doi.org/10.1038/nmeth1030

40 Ono, T., Isobe, K., Nakada, K. and Hayashi, J.-I. (2001) Human cells are protected from mitochondrial dysfunction by complementation of DNA products in fused mitochondria. *Nat. Genet.* **28**, 272–275 https://doi.org/10.1038/90116

41 Davis, A.F. and Clayton, D.A. (1996) In situ localization of mitochondrial DNA replication in intact mammalian cells. *J. Cell Biol.* **135**, 883–893 https://doi.org/10.1083/jcb.135.4.883

42 Imamura, H., Nhat, K.P.H., Togawa, H., Saito, K., Iino, R., Kato-Yamada, Y. et al. (2009) Visualization of ATP levels inside single living cells with fluorescence resonance energy transfer-based genetically encoded indicators. *Proc. Natl Acad. Sci. U.S.A.* **106**, 15651–15656 https://doi.org/10.1073/pnas.0904764106

43 Twig, G., Elorza, A., Molina, A.J.A., Mohamed, H., Wikstrom, J.D., Walzer, G. et al. (2008) Fission and selective fusion govern mitochondrial segregation and elimination by autophagy. *EMBO J.* **27**, 433–446 https://doi.org/10.1038/sj.emboj.7601963

44 Hoitzing, H., Johnston, I.G. and Jones, N.S. (2015) What is the function of mitochondrial networks? A theoretical assessment of hypotheses and proposal for future research. *BioEssays* **37**, 687–700 https://doi.org/10.1002/bies.201400188

45 Whitfield, M.L., Sherlock, G., Saldanha, A.J., Murray, J.I., Ball, C.A., Alexander, K.E. et al. (2002) Identification of genes periodically expressed in the human cell cycle and their expression in tumors. *Mol. Biol. Cell* **13**, 1977–2000 https://doi.org/10.1091/mbc.02-02-0030

46 Murphy, M.P. (2009) How mitochondria produce reactive oxygen species. *Biochem. J.* **417**, 1–13 https://doi.org/10.1042/BJ20081386

47 Brodie, A.E. and Reed, D.J. (1990) Cellular recovery of glyceraldehyde-3-phosphate dehydrogenase activity and thiol status after exposure to hydroperoxides. *Arch. Biochem. Biophys.* **276**, 212–218 https://doi.org/10.1016/0003-9861(90)90028-W

48 Knight, R.J., Kofoed, K.F., Schelbert, H.R. and Buxton, D.B. (1996) Inhibition of glyceraldehyde-3-phosphate dehydrogenase in post-ischaemic myocardium. *Cardiovasc. Res.* **32**, 1016–1023 https://doi.org/10.1016/S0008-6363(96)00137-X

49 Danielson, S.R., Carelli, V., Tan, G., Martinuzzi, A., Schapira, A.H.V., Savontaus, M.-L. et al. (2005) Isolation of transcriptomal changes attributable to LHON mutations and the cybridization process. *Brain* **128**, 1026–1037 https://doi.org/10.1093/brain/awh447

50 Hao, H., Morrison, L.E. and Moraes, C.T. (1999) Suppression of a mitochondrial tRNA gene mutation phenotype associated with changes in the nuclear. *Hum. Mol. Genet.* **8**, 1117–1124 https://doi.org/10.1093/hmg/8.6.1117

51 Wilkins, H.M., Carl, S.M. and Swerdlow, R.H. (2014) Cytoplasmic hybrid (cybrid) cell lines as a practical model for mitochondriopathies. *Redox Biol.* **2**, 619–631 https://doi.org/10.1016/j.redox.2014.03.006

52 Otten, A.B.C., Theunissen, T.E.J., Derhaag, J.G., Lambrichs, E.H., Boesten, I.B.W., Winandy, M. et al. (2016) Differences in strength and timing of the mtDNA bottleneck between zebrafish germline and non-germline cells. *Cell Rep.* **16**, 622–630 https://doi.org/10.1016/j.celrep.2016.06.023

53 Goto, Y.-i., Nonaka, I. and Horai, S. (1990) A mutation in the tRNALeu (UUR) gene associated with the MELAS subgroup of mitochondrial encephalomyopathies. *Nature* **348**, 651–653 https://doi.org/10.1038/348651a0

54 Viscomi, C., Bottani, E., Civiletto, G., Cerutti, R., Moggio, M., Fagiolari, G. et al. (2011) *In vivo* correction of COX deficiency by activation of the AMPK/PGC-1α axis. *Cell Metab.* **14**, 80–90 https://doi.org/10.1016/j.cmet.2011.04.011

55 Jain, I.H., Zazzeron, L., Goli, R., Alexa, K., Schatzman-Bone, S., Dhillon, H. et al. (2016) Hypoxia as a therapy for mitochondrial disease. *Science* **352**, 54–61 https://doi.org/10.1126/science.aad9642

56 Bough, K.J., Wetherington, J., Hassel, B., Pare, J.F., Gawryluk, J.W., Greene, J.G. et al. (2006) Mitochondrial biogenesis in the anticonvulsant mechanism of the ketogenic diet. *Ann. Neurol.* **60**, 223–235 https://doi.org/10.1002/ana.20899

57 Ahola-Erkkilä, S., Carroll, C.J., Peltola-Mjösund, K., Tulkki, V., Mattila, I., Seppänen-Laakso, T. et al. (2010) Ketogenic diet slows down mitochondrial myopathy progression in mice. *Hum. Mol. Genet.* **19**, 1974–1984 https://doi.org/10.1093/hmg/ddq076

58 Steriade, C., Andrade, D.M., Faghfoury, H., Tarnopolsky, M.A. and Tai, P. (2014) Mitochondrial encephalopathy with lactic acidosis and stroke-like episodes (MELAS) may respond to adjunctive ketogenic diet. *Pediatr. Neurol.* **50**, 498–502 https://doi.org/10.1016/j.pediatrneurol.2014.01.009

Supplementary Information

Text S1

Transformation to Per-Cell Dimensions using Cell Volume

In this section we show that it is necessary to multiply measurements of protein and mRNA levels, when determined by Western blot and RNA-seq respectively, by cell volume to transform the data to mean cellular measurements.

Consider a Western blot experiment determining the levels of a gene (gene i) in two conditions (A and B). Denote the number of proteins per cell of gene i, as n_i^A, where the superscript denotes condition A. Let us also denote the total number of proteins per cell as N^A.

When one performs a Western blot, the protein of interest is stained with an antibody, cells are lysed, and a sample of fixed protein mass (m) is taken from the lysate. If we denote the number of proteins for the gene of interest in the sample as P_i^A, then we may write

$$P_i^A = \frac{n_i^A}{N^A} m, \tag{S1}$$

since the proportion of protein i in the sample is determined by the proportion of protein i in the proteome (n_i^A/N^A). Western blot experiments also tend to be normalised by a loading control (c), so the normalised measurement we have access to is

$$\frac{P_i^A}{P_c^A} = \frac{n_i^A}{n_c^A} \tag{S2}$$

which corresponds to the data given in Picard et al. [13].

Now, consider a perturbation in condition B, causing the amount of protein for gene i to be n_i^B, and the mean cell volume to experience a fold-change V_f, as in Figure S12. Consequently, $N^B = V_f N^A$, since total protein content scales with the volume of the cell. Using the reasonable assumption that the loading control is a gene whose expression also scales with cell volume (e.g. β-actin, as in Picard et al. [13]), then $n_c^B = V_f n_c^A$. It follows that

$$\frac{P_i^B}{P_c^B} = \frac{n_i^B}{V_f n_c^A}. \tag{S3}$$

Then, if we are interested in the relative fold-change expression of the protein between the two conditions, then we take the ratio

$$\frac{P_i^B/P_c^B}{P_i^A/P_c^A} = \frac{n_i^B/n_c^A}{n_i^A/n_c^A} \cdot \frac{1}{V_f} = \frac{n_i^B}{n_i^A} \cdot \frac{1}{V_f} \tag{S4}$$

Thus, the quantity on the left hand side of Eq. (S4), which is what one usually measures in a Western blot, has a multiplicative-bias of $1/V_f$. Therefore, if one is interested in per-cell protein changes, the appropriate quantity of interest is

$$\frac{P_i^B/P_c^B}{P_i^A/P_c^A} \cdot V_f. \tag{S5}$$

Hence, we multiply each protein measurement by $V(h) \equiv V_f(h) = \langle V_k(h) \rangle_k / \langle V_k(h=0) \rangle_k$, where $\langle \dots \rangle_k$ denotes the sample mean over technical replicates k, such that $V(0) = 1$.

A similar argument applies to RNA-seq data, since a fixed mass of mRNA is extracted for an RNA-seq experiment, so an analogous pair of equations to Eq.(S1) in conditions A and B holds. Using the assumption that $N^B = V_f N^A$, and denoting the number of mRNA molecules in each sample with M, it can be shown that

$$\frac{M_i^B}{M_i^A} = \frac{n_i^B}{n_i^A} \cdot \frac{1}{V_f}. \tag{S6}$$

Text S2

Generative Model Description

We used a Bayesian framework to find the supported parameter values given the data, using the Metropolis-Hastings algorithm [1]. To do this, we included an additional 6 noise parameters, for the features where parameter inference was performed (i.e. all of the features except N^+, which has no free parameters, see

Eq.(4)). For these 6 features ($M_{\mathrm{ETC}}, P^+, M_{\mathrm{gly}}, V, G, R_{\mathrm{max}}$), we assumed that the data were generated subject to Gaussian noise.

Thus, the full statistical model contains 12 parameters (excluding 6 noise parameters for each feature), with 32 data points which enter the likelihood (after excluding $h = 1$ data). To summarise, counting the 6 features which have free parameters, the model consists of $12/6 = 2$ mean parameters per feature, on average. Note that simply fitting linear models to the 6 features in Fig. 1 would also require 2 parameters per feature. The model fit is shown in Fig. 3.

To connect our model of mean cellular behaviour $\mathcal{S} = \{M_{\mathrm{ETC}}, P^+, M_{\mathrm{gly}}, V, G, R_{\mathrm{max}}\}$, to the data of Picard *et al.* [13], we assume that the sample mean of feature i ($y_{i,j}$) at a discrete value of heteroplasmy $h = j$ is generated via Gaussian noise ($\mathcal{N}(\mu, \sigma)$) whose mean corresponds to one of the models $\mathcal{S}$,

$$y_{i,j} = \mathcal{M}_i(h) + \mathcal{N}(0, \sigma_i), \tag{S7}$$

where $\mathcal{M}_i(h)$ is an element from the set of models $\mathcal{S}$. We stress that the data we train our model on, $y_{i,j}$, is the *sample mean*, rather than the raw data. This is a less common approach; however, we believe that it is appropriate as individual replicates only give us information on the technical variability measured in [13], whereas the total error is a combination of both technical and biological variability. Training our models on individual replicates would be likely to underestimate the true variability of the data, so we favoured training on the sample mean only. This raises the challenge of establishing an appropriately permissive model for our uncertainty in σ_i.

We can infer the distribution of the parameters (θ) of the models $\mathcal{S}$, given the data $y_{i,j}$, using Bayes rule and a prior distribution over θ ($P(\theta)$)

$$P(\theta|y_{i,j}) = \frac{P(y_{i,j}|\theta)P(\theta)}{P(y_{i,j})}. \tag{S8}$$

The log-likelihood in this case is

$$\log[P(y_{i,j}|\theta)] = \sum_{i,j} -1/2\log(2\pi) - \log(\sigma_i) - \frac{1}{2}\left(\frac{y_{i,j} - \mathcal{M}_i(j)}{\sigma_i}\right)^2. \tag{S9}$$

We drop the constant $\sum_{i,j} -1/2\log(2\pi)$ from our log-likelihood, since we will only be interested in differences in the log-likelihood to perform Bayesian inference using the Metropolis-Hastings algorithm [1].

We used exponential priors σ_i

$$P(\sigma_i) \propto \exp(-\lambda_i \sigma_i) \tag{S10}$$

as our error model. The constant λ_i was chosen such that the scale of decay of probability was on the same scale as the range of the data. Noting that $\langle P(\sigma_i)\rangle = 1/\lambda_j$, we chose

$$\lambda_i = \frac{\Omega}{\max_j\{\hat{y}_{i,j}\} - \min_j\{\hat{y}_{i,j}\}} \tag{S11}$$

where Ω is a hyper-parameter of the prior and $\Omega \geq 0$. Note that we may interpret $\Omega = 0$ as an improper uniform prior, since $P(\sigma_i) = \text{const}$ in this case.

We began with $\Omega = 0$ as the most permissive choice of prior possible, given the model in Eq.(S10). We found that when $\Omega = 0$ *the maximum a posteriori estimates were qualitatively similar* to choosing $\Omega = 2$ (our final choice which we justify below) see Fig. 3 ($\Omega = 2$) and Figure S13A-F ($\Omega = 0$). However, we found that the posterior 25-75% credible interval supported model fits for M_{ETC}, P^+ and R_{max} which were relatively poor when $\Omega = 0$, compared to $\Omega = 2$ (see Figure S13A-F). We determined that large values of h^* were indicative of purely linear fits to the data, which is unlikely given the wider body of evidence demonstrating the nonlinearity of the threshold effect. This is seen in Figure S13G-L (high h^*, poorer fit) when compared with Figure S13M-R (low h^*, better fit). Comparison between Figure S13G and Figure S13M is particularly noteworthy, where the 25-75% posterior credible interval for high h^* sub-samples predicts $M_{\mathrm{ETC}} \approx 0$ for all values of h, which is physiologically implausible, whereas low h^* sub-samples display non-linear fits which more faithfully track the data. Figure S14 shows that the high h^* mode is of comparable prevalence to the low h^* mode when $\Omega = 0$.

We therefore investigated the sensitivity to choice in Ω in Figure S14. We see that increasing Ω reduces the width of the marginal posterior distribution of h^*, constraining the posterior distribution to lie around

the nonlinear solutions shown in Fig. 3. We found that the permissive prior $\Omega = 2$ was sufficient to strongly subdue this, physiologically implausible, large h^* mode. This can be interpreted as a prior belief that our model uncertainty is, on average, 50% of the range of the data (since $\langle P(\sigma_i)\rangle = \lambda_i^{-1}$). We believe this to be a sensible prior choice, encoding our prior belief that the threshold effect is nonlinear while providing only a gentle constraint on parameters.

We favoured uniform priors on the remaining parameters so that the posterior would be dominated by the likelihood. However, a number of the parameters in the model were uncertain over orders of magnitude; in these cases, we allowed the log of these parameters to take uniform distributions. Explicitly, our priors were chosen as:

$$P(h^*) = \text{unif}(0, 1) \tag{S12}$$
$$P(\ln(k_{\text{mRNA}})) = \text{unif}(-10\ln 10, 2\ln 10) \tag{S13}$$
$$P(f_m) = \text{unif}(0, 1) \tag{S14}$$
$$P(\ln(k_m)) = \text{unif}(-10\ln 10, 2\ln 10) \tag{S15}$$
$$P(\ln(\delta_p)) = \text{unif}(-10\ln 10, 2\ln 10) \tag{S16}$$
$$P(\ln(k_o)) = \text{unif}(-10\ln 10, 2\ln 10) \tag{S17}$$
$$P(\ln(k_g)) = \text{unif}(-10\ln 10, 2\ln 10) \tag{S18}$$
$$P(c_1) = \text{unif}(-10, 10) \tag{S19}$$
$$P(m_2) = \text{unif}(0, 100) \tag{S20}$$
$$P(k_{gr}) = \text{unif}(0, 100) \tag{S21}$$
$$P(\ln(k_p)) = \text{unif}(-10\ln 10, 2\ln 10). \tag{S22}$$

The ranges for h^* and f_m are justified since these quantities can physically only be between 0 and 1. c_1 and m_2 are parameters of linear models for M_{gly} (see Table S1 and Eq.(8)) for data which has been normalized to the scale of 1; therefore priors were chosen with suitably large ranges. Similarly for k_{gr}, a proportionality constant relating growth to cell volume ((see Table S1 and Eq.(10)), we expect k_{gr} to be of the order of 1, since the data has been normalized, and chose suitably relaxed priors. The ranges for all other parameters, which were sampled in log-space due to our greater uncertainty of their values, were chosen to be suitably large as to be unlikely to reach the boundary of the prior during sampling with MCMC.

The parameters β and k_{mRNA} from Eq.(5) were highly correlated. For more efficient chain mixing, we rearranged Eq.(5) into the form

$$M_{\text{ETC}} = \frac{\zeta}{\frac{1}{k_{\text{mRNA}}} + \frac{1}{1+\exp[k_m(h-h_0)]}}, \tag{S23}$$

where $\zeta = \beta/k_{\text{mRNA}}$, and used the prior

$$P(\ln(\zeta)) \sim \text{unif}(-10\ln 10, 2\ln 10) \tag{S24}$$

such that the boundaries for the uniform prior were relatively relaxed.

We performed the Metropolis-Hastings algorithm [1] to sample from the posterior, using a Gaussian random walk as our transition kernel, whose covariance matrix was determined from a trial run of the adaptive Metropolis algorithm [3]. All code was written in either Python or C, and is available upon request. The MCMC chain trajectory is presented in Figure S7.

Text S3

Justification of ETC mRNA and protein

Consider a *single* molecule of wild-type mtDNA which, when transcribed, generates mRNA for the electron transport chain (ETC), which we denote as m_{ETC}. Transcripts are generated according to a deterministic process (stochasticity in gene expression [4] is neglected in this picture) with rate (β) and also passively degrade at some basal rate (δ_m^b). We consider a controlled, active degradation process (δ_m^a) that acts in addition to the background level. Thus, at the single mtDNA level, we may write down the differential equation

$$\frac{\mathrm{d}m_{\text{ETC}}}{\mathrm{d}t} = \beta - \left(\delta_m^a + \delta_m^b\right) m_{\text{ETC}}, \tag{S25}$$

where we assume that β, δ_m^b are constant.

Control of the expression levels of different mitochondrial genes is manifest at the level of mRNA degradation [28], because mtDNA is transcribed as a single polycistronic transcript [27]. We therefore use the simplifying assumption that, in the pathogenic case, mitochondrial mRNA is also controlled at the level of degradation. Thus we allow the active degradation to vary with heteroplasmy $\delta_m^a = \delta_m^a(h)$, and assume the transcription rate to be constant.

Cells are measured at steady-state, so setting the derivative to zero yields

$$m_{\mathrm{ETC}} = \frac{\beta}{\delta_m^a + 1}, \tag{S26}$$

where δ_m^b has been absorbed into the definitions of β and $\delta_m^a(h)$. Assuming N^+ scaling, whereby only wild-type mtDNAs contribute to the transcript pool, we arrive at an expression for *cellular* levels of ETC mRNA:

$$M_{\mathrm{ETC}} = \frac{\beta}{\delta_m^a + 1} N^+.$$

Dropping the a superscript yields Eq.(5).

Note that, in our Bayesian inference, we chose to express the constant h_0 in Eq.(6) in terms of the critical heteroplasmy h^* using the expression $h_0 = h^* - \ln[(1 - f_m)/f_m]/k_m$, where $0 < f_m \leq 1$. This simply expresses the location of h^* in terms of the fraction f_m of the sigmoid's maximal value. Intuitively, if f_m and k_m are sufficiently large, h^* signals the beginning of reduction in ETC degradation.

For ETC protein, we assume that the following equation holds at the cellular level

$$\frac{\mathrm{d}P^+}{\mathrm{d}t} = \lambda M_{\mathrm{ETC}} N^+ - \delta_p^b P^+ \tag{S27}$$

where $\lambda = \mathrm{const}$, and we assume there is no active degradation of ETC protein. At steady-state

$$P^+ = \frac{M_{\mathrm{ETC}} N^+}{\delta_p^b} \tag{S28}$$

where λ is absorbed into the definition of δ_p^b. Dropping the b superscript yields Eq. (7).

Justification of cell volume scaling for power demand

A reasonable general model for the way in which power demands of a mammalian cell scale with its volume (V) is $k_1 V + k_2 V^{2/3} + K + f(N, V)$, where k_i are proportionality constants. Each term may be interpreted as: $k_1 V$ are demands which scale with cell volume; $k_2 V^{2/3}$ scale with cell surface area; K are demands which are constant for a cell (for example, the cost of replicating the genome); and $f(N, V)$ is an unknown function corresponding to proton leak, which potentially depends upon mitochondrial mass (or alternatively mtDNA copy number, N) and cell volume. These are the dominant power demands of mammalian cells, as determined by [24–26].

Many energy-consuming processes in mammalian cells directly depend upon cell size; for example, a model system used by Buttgereit *et al.* found that ∼30% of oxygen consumption corresponded to plasma membrane transporters, and ∼20% corresponded to protein synthesis [24]. We assume that protein synthesis scales proportionally with V, because 60% of total cellular dry mass is protein [10] and mass scales with volume. Also, we may assume that plasma membrane power consumption scales with cell surface area, which scales with $V^{2/3}$. By using volume and surface area contributions alone, we may account for ∼50% of the power demands of the cell, which is 63% of the accountable power demands for this model system since only 80% of total respiration rate could be attributed to particular processes in their study [24].

Thus, assuming that all power consumption is due to surface area or volume contributions then, using the data of [24], a reasonable model for power demand might be $f(V) = 0.4V + 0.6V^{2/3}$, the volume parameter being $20/(20 + 30) = 0.4$. However, we see in Fig. 1D that the normalized volume data lie in the range $0.6 \lesssim V \lesssim 1$. In this region, the functions $f(V)$ and $g(V) = V$ are similar, with a difference of no more than ∼7%. Thus, $g(V) = V$ is a reasonable approximation for total power demands in this case.

We note, however, that the above proportions depend on the environment of the cell [24, 25] as well as the tissue type (reviewed in [26]), often showing variation on the order of tens of percent. In light of this uncertainty, and for the sake of parsimony, we make the simplifying assumption that total power demand scales purely with cell volume, see Eq.(9).

Expected cell volume and growth rate

Two of the simplest models for how cells may grow throughout the cell cycle are linear and exponential growth. We show below that a relationship exists between growth rate and the mean cell volume in an asynchronous population of cells under a linear model. Furthermore, assuming an exponential model, growth rate and mean cell volume are independent.

Firstly, we assume that the number of cells obey a pure-birth process, in other words the death rate of cells is negligible. If the initial number of cells (N_0) is large, then we can use a deterministic model of cell growth, $N(t) = N_0 \exp(Gt)$, where $N(t)$ is the number of cells at time t and G is the growth rate of cells, as described in Eq.(10). Assuming that the number of cells doubles every cell cycle period (t_d), then

$$G = \frac{\ln(2)}{t_d}. \tag{S29}$$

Under a linear model of cytoplasmic growth through the cell cycle, the volume of an individual cell may be written as

$$V_c(t) = V_0 + \lambda t \tag{S30}$$

where V_c is the volume of an individual cell, V_0 is the volume of a cell just after division (assumed to be constant for all cells) and $\lambda = V_0/t_d = \text{const}$ is the cytoplasmic growth rate. We note that, by our assumption of $\lambda = \text{const}$ and a linear growth model, smaller cells require less time to double in volume and consequently will proliferate faster (as shown below). From an energetics perspective, a simple model is that cellular power demand relating to proliferation scales with λ, i.e. more energy per unit time is required to increase the cytoplasmic growth rate. Since we model $\lambda = \text{const}$, we expect power demands associated with proliferation to also be constant regardless of the volume of the cell (and hence independent of heteroplasmy in the model presented in the Main Text). We use the parsimonious ansatz that this power demand is small relative to the power demands of maintaining cytoplasmic volume, and hence we neglect a λ-dependent term in Eq.(6).

In an asynchronous population, we assume that each cell is distributed uniformly through the cell cycle, in other words

$$T \sim \text{unif}(0, t_d) \tag{S31}$$

where T is a random variable describing the position in time, of a cell in its cell cycle.

We wish to find the expected value of cell volume, ($\mathbb{E}(V_c) \equiv V$, as described in Eq.(9)), given the assumption of Eq.(S31). Eq.(S30) can be viewed as a transformation of the random variable T. If X is a continuous random variable, then for any transformation $Y = r(X)$, $\mathbb{E}(Y) = \int r(x)P(x)\mathrm{d}x$, where $P(x)$ is the probability distribution corresponding to the random variable X [11]. This implies that $\mathbb{E}(V_c) = 1/t_d \int_0^{t_d} V_c(t)\mathrm{d}t$. For Eq.(S30), this yields $\mathbb{E}(V_c) = 3V_0/2$, but since $V_0 = \lambda t_d$, then Eq.(S29) yields

$$G = \frac{3\lambda \ln(2)}{2\mathbb{E}(V)}, \tag{S32}$$

i.e. $1/G \propto \mathbb{E}(V) \equiv V$.

If, however, we assume an exponential model of cell growth through the cell cycle

$$V_c(t) = V_0 \exp(\gamma t) \tag{S33}$$

then $t_d = \ln(2)/\gamma$ and $\mathbb{E}(V_c) = V_0/\ln(2)$ which cannot be written in terms of t_d and therefore G is independent of V.

The above makes intuitive sense: if a cell grows linearly, then a larger cell will need more time to double in size than a smaller cell, if their growth rates are the same. On the other hand, if a cell grows exponentially, then regardless of its initial size, the doubling time is constant, given a fixed cytoplasmic growth rate.

Since there is presumably a wide class of cell growth dynamics where cell size is dependent on growth rate, we favoured a linear model for its simplicity. Measurements by Tzur *et al.* show that, on average, under both a linear and exponential model of cytoplasmic volume growth, the rate constant varies with time [12]. However, the implication of this for the relationship between V and G remains unclear.

Text S4

Below, we will propose potential experiments to test the corresponding claims made in Key Claims and Predictions of Biophysical Model of Heteroplasmy.

Wild-type mtDNA density homeostasis is maintained until a minimum volume is reached at the critical heteroplasmy

If N^+/V is a quantity kept under homeostasis, then under wild-type conditions, perturbations to mtDNA copy number may be expected to cause changes in cell volume. This might be testable by reducing mtDNA copy number with chemicals such as ddC, or increasing it through PGC-1α overexpression, which, in the absence of other homeostatic effects, we expect to reduce and increase mean cell volume respectively.

A second testable prediction is that a minimum cell volume (V_{min}) causes bioenergetic toggling at h^*. We should be aware of the two potential interpretations of V_{min} raised: (1) bioenergetic and (2) mechanical. If V_{min} is bioenergetic, then raising the power demands of the cell which do not scale with volume, may induce h^* to be encountered earlier. This could be achieved by increasing the amount of DNA in the nucleus which must be replicated, creating a one-time cost to the cell per cell cycle. This is not expected to affect any mechanical constraints since DNA content is not directly indicative of nuclear size [13]. Ideally, the amount of DNA introduced should be large (i.e. billions of base pairs), be replicated, and not interfere with normal functioning of the nucleus. This could be achieved by chemically inducing polyploidy, for instance by using Noscapine [14]. The location of h^* could again be determined by performing RNA-seq, and observing the upregulation of glycolysis with heteroplasmy.

If increasing the power demands of the nucleus yields no change in the distribution of h^*, then a mechanical constraint could be more relevant. This could be tested by perturbing cell volume. Reducing cell volume under this hypothesis is expected to shift h^* to lower values of heteroplasmy, which could be determined via RNA-seq.

Mitochondrial tRNAs are enriched in the vicinity of their corresponding parental mtDNA

The spatial distribution of mitochondrial tRNAs relative to mtDNA would be most directly determined by fluorescent labelling of mitochondrial tRNA and mtDNA. MtDNA labelling could be achieved through picoGreen staining [15]. Labelling of processed tRNAs within mitochondria is more difficult, but methods exist for labelling mRNA in both fixed cells [16] and dynamically [18, 39] within mitochondria, which may be informative. The experimental suggestion put forward Busch *et al.* [36] to probe the strength of the genotype-phenotype link, via super-resolution microscopy [20], by determining the existence of focal deficiencies in ETC protein concentration would also be illuminating.

Mutant mtDNAs have a transcriptional defect

If mutant mtDNAs have a transcription defect, then the abundance of mRNA encoding mutant tRNAs relative to mRNA encoding wild-type tRNAs would be expected to be smaller than h. This measurement could be performed by RT-qPCR, with probes which target the single-nucleotide polymorphism associated with the 3243A>G mutation, to probe the ratio of mRNA derived from mutant and wild-type mtDNAs. Superresolution microscopy to determine the existence of focal deficiencies in ETC protein would also potentially indicate the existence of a local genotype-phenotype link, which would support this hypothesis [20, 36].

Cell volume is not explained by cell cycle variations

To separate the potential confounding influence of the cell cycle on mean cell size, heteroplasmic cells could be transfected with Fucci markers [21], and relative enrichment of cell cycle stages determined.

Cells proliferate inversely with their size

To determine the dependence of growth rate on mean cell volume, wild-type cells could be synchronised, and sorted by their volume. These cells could then be plated and released from synchronisation, and the growth rate of cells measured similar to that described in Materials and Methods. Synchronisation is necessary, because cell volume is expected to vary by a factor of 2 through the cell cycle, so any sorting would otherwise be strongly confounded by the cell cycle. A potential alternative to synchronisation, which can be stressful to cells, is to label genes associated with a particular stage of the cell cycle, and sort based on both this fluorescence signal and cell volume.

Maximum respiratory capacity linearly tracks ETC protein content

Measurements of maximum respiratory capacity at $h = 0$, as well as measurement of ETC protein levels at $h = 0.6$ and $h = 0$, may help determine whether a simple linear relationship is sufficient, or whether a more complex model is justified.

Summary

A summary of the experimental proposals outlined are given in Table S2

Text S5

Alternative models: Mutant mtDNA and transcription

Eq.(5) states that mutant mtDNAs do not contribute significantly to the transcript pool. We can relax this constraint by replacing Eq.(5) with

$$M_{\mathrm{ETC}} = \frac{\beta}{\delta_m + 1}(N^+ + \mu N^-) \tag{S34}$$

where $0 \leq \mu \leq 1$ and $N^- = hN$, where N is the total number of mtDNAs, which we treat as a constant.

Using the uniform prior

$$P(\mu) = \mathrm{unif}(0, 1), \tag{S35}$$

we sampled from the posterior, as described in Text S2. The MCMC trajectory is shown in Figure S8. The marginal posterior density for μ in Figure S8, shows that $\mu \approx 1$ is the most likely value of the parameter, in other words mutant mtDNAs contribute equally to the transcript pool, compared to wild-type molecules. However, draws from the posterior distribution of M_{ETC} were often purely linear and thus inappropriate for understanding threshold effects (see Figure S16). We consequently rejected this model in favour of the model presented in the main text.

Alternative models: tRNA misincorporation model

Eq.(7) states that ETC protein is generated when ETC mRNA is in contact with wild-type mtDNA, suggesting that tRNAs affected by the MELAS mutation, leucine-UUR, remain local to their parent mtDNAs. The alternative is that mitochondrial tRNAs are well diffused amongst mitochondrial mRNAs. If we assume that a mutant tRNA causes a misincorporation during translation with 100% efficiency, then the number of misincorporations per protein follows a binomial distribution. We assume that the probability of a single misincorporation is h. We further assume that proteins have a mutational tolerance of x misincorporations, or less, before they are considered mutated (and consequently degraded). With these assumptions, the expected proportion of mutant proteins (m_p) will be

$$m_p = 1 - F(x|N, h) \tag{S36}$$

where N is the number of leucine-UUR residues per protein, and $F(x|N, h) = P(X \leq x)$ is the cumulative distribution function of the binomial distribution, for N trials, x successes, and probability of success h. A plot of m_p is given in Figure S11, for different mutational tolerances x against heteroplasmy.

We can therefore use an analogous expression to Eq.(7) for P^+, in the case of well-diffused tRNAs

$$P^+ = \frac{M_{\mathrm{ETC}} F(x|N, h)}{\delta_p^b}. \tag{S37}$$

By replacing Eq.(7) with Eq.(S37), we again sampled from the posterior as described in Text S2. We chose $N = 8$, which is the average number of susceptible residues in the 11 mitochondrially-encoded subunits considered (see caption of Fig. 1) [9]. Our prior for the unknown tolerance to misincorporations, x, was chosen as a discrete uniform prior

$$P(x) = \begin{cases} \frac{1}{9}, & x = 0, 1, \ldots, 8 \\ 0, & \text{otherwise.} \end{cases} \tag{S38}$$

The MCMC trajectory is shown in Figure S9, and the model fit in Figure S11. Draws from the posterior distribution of M_{ETC} were often purely linear and thus inappropriate for understanding threshold effects

(see Figure S16). We consequently rejected this model, in favour of the model presented in the main text. Furthermore, observing the marginal posterior distribution of the misincorporation tolerance x in Figure S9, we see that the most likely value of the parameter is $x = N = 8$. In other words, ETC proteins are immune to the MELAS mutation, which we believe to be incorrect [9]. For these reasons, we rejected this model in favour of the model presented in the main text.

Text S6

Relative OXPHOS contribution to power supply

It is interesting to observe the relative contributions of oxidative phosphorylation and glycolysis to power supply. Since Eq.(9) states that power supply = demand, where demand corresponds to cell volume, the ratio $f_o = k_o P^+/V$ determines the relative contribution of OXPHOS to power supply, see Figure S15.

For $h < h^*$, we see that OXPHOS has decreasing contributions to power supply. At h^*, OXPHOS contributions stabilize with $0.28 < f_o(h = 0.52 \approx h^*_{\mathrm{MAP}}) < 0.44$ (25-75% CI). The heteroplasmy at which OXPHOS contributions are stabilized corresponds to the hypothesized demand/supply toggle, where the cell attempts to increase power supply as opposed to reducing power demand.

The value of f_o where OXPHOS contributions become stabilized ($f_o(h^*)$) may have wider significance. Mitochondrial metabolism, and especially mitochondrial membrane potential, is connected to a variety of biosynthetic pathways [1] and crucial for maintaining cellular proliferation [14]. $f_o(h^*)$ may represent a minimum ETC flux, relative to power demand, for mitochondria to support their mitochondrial membrane potential without the aid of glycolytic ATP. Below $f_o(h^*)$, we might predict that cells run ATP synthase in reverse, hydrolysing glycolytic ATP to maintain membrane potential.

References

1. Hastings, W.K. (1970) Monte Carlo sampling methods using Markov chains and their applications *Biometrika* **57**, 97–109

2. Picard, M., Zhang, J., Hancock, S., Derbeneva, O., Golhar, R., Golik, P., O'Hearn, S., Levy, S., Potluri, P., Lvova, M. et al. (2014) Progressive increase in mtDNA 3243A > G heteroplasmy causes abrupt transcriptional reprogramming *Proc. Natl Acad. Sci. USA* **111**, E4033–E4042

3. Haario, H., Saksman, E., and Tamminen, J. (2001) An adaptive Metropolis algorithm *Bernoulli* **7**, 223–242

4. Elowitz, M.B., Levine, A.J., Siggia, E.D., and Swain, P.S. (2002) Stochastic gene expression in a single cell *Science* **297**, 1183–1186

5. Chujo, T., Ohira, T., Sakaguchi, Y., Goshima, N., Nomura, N., Nagao, A., and Suzuki, T. (2012) LRPPRC/SLIRP suppresses PNPase-mediated mRNA decay and promotes polyadenylation in human mitochondria *Nucleic Acids Res.* **40**, 8033–8047

6. Ojala, D., Montoya, J., and Attardi, G. (1981) tRNA punctuation model of RNA processing in human mitochondria *Nature* **290**, 470–474

7. Buttgereit, F., Brand, M., and Müller, M. (1992) ConA induced changes in energy metabolism of rat thymocytes *Biosci. Rep.* **12**, 109–114

8. Brand, M.D., Couture, P., Else, P.L., Withers, K.W., and Hulbert, A. (1991) Evolution of energy metabolism. Proton permeability of the inner membrane of liver mitochondria is greater in a mammal than in a reptile *Biochem. J.* **275**, 81–86

9. Rolfe, D. and Brown, G.C. (1997) Cellular energy utilization and molecular origin of standard metabolic rate in mammals *Physiol. Rev.* **77**, 731–758

10. Alberts, B., Johnson, A., Lewis, J., Roberts, K., Raff, M., and Walter, P. (2002) *Molecular Biology of the Cell* Garland Science

11. Wasserman, L. (2013) *All of Statistics: A Concise Course in Statistical Inference* Springer Texts in Statistics Springer New York

12. Tzur, A., Kafri, R., LeBleu, V.S., Lahav, G., and Kirschner, M.W. (2009) Cell growth and size homeostasis in proliferating animal cells *Science* **325**, 167–171

13. Neumann, F.R. and Nurse, P. (2007) Nuclear size control in fission yeast *J. Cell Biol.* **179**, 593–600

14. Schuler, M., Muehlbauer, P., Guzzie, P., and Eastmond, D. (1999) Noscapine hydrochloride disrupts the mitotic spindle in mammalian cells and induces aneuploidy as well as polyploidy in cultured human lymphocytes *Mutagenesis* **14**, 51–56

15. Bereiter-Hahn, J. and Vöth, M. (1998) Distribution and dynamics of mitochondrial nucleoids in animal cells in culture in *Experimental Biology Online* Springer 58–77

16. Alán, L., Zelenka, J., Ježek, J., Dlasková, A., and Ježek, P. (2010) Fluorescent in situ hybridization of mitochondrial DNA and RNA *Acta Biochim. Pol.* **57**, 403

17. Ozawa, T., Natori, Y., Sato, M., and Umezawa, Y. (2007) Imaging dynamics of endogenous mitochondrial RNA in single living cells *Nature Methods* **4**, 413–419

18. Chatre, L. and Ricchetti, M. (2013) Large heterogeneity of mitochondrial DNA transcription and initiation of replication exposed by single-cell imaging *J. Cell Sci.* **126**, 914–926

19. Busch, K.B., Kowald, A., and Spelbrink, J.N. (2014) Quality matters: how does mitochondrial network dynamics and quality control impact on mtDNA integrity? *Phil. Trans. R. Soc. B* **369**, 20130442

20. Wilkens, V., Kohl, W., and Busch, K. (2013) Restricted diffusion of OXPHOS complexes in dynamic mitochondria delays their exchange between cristae and engenders a transitory mosaic distribution *J Cell Sci* **126**, 103–116

21. Sakaue-Sawano, A., Kurokawa, H., Morimura, T., Hanyu, A., Hama, H., Osawa, H., Kashiwagi, S., Fukami, K., Miyata, T., Miyoshi, H. et al. (2008) Visualizing spatiotemporal dynamics of multicellular cell-cycle progression *Cell* **132**, 487–498

22. Ahn, C.S. and Metallo, C.M. (2015) Mitochondria as biosynthetic factories for cancer proliferation *Cancer Metab* **3**, 1 doi:10.1186/s40170-015-0128-2

23. Martínez-Reyes, I., Diebold, L.P., Kong, H., Schieber, M., Huang, H., Hensley, C.T., Mehta, M.M., Wang, T., Santos, J.H., Woychik, R. et al. (2015) TCA Cycle and Mitochondrial Membrane Potential Are Necessary for Diverse Biological Functions *Mol. Cell* **61**, 199–209

24. Sasarman, F., Antonicka, H., and Shoubridge, E.A. (2008) The A3243G tRNALeu (UUR) MELAS mutation causes amino acid misincorporation and a combined respiratory chain assembly defect partially suppressed by overexpression of EFTu and EFG2 *Hum. Mol. Genet.* **17**, 3697–3707

25. Whitfield, M.L., Sherlock, G., Saldanha, A.J., Murray, J.I., Ball, C.A., Alexander, K.E., Matese, J.C., Perou, C.M., Hurt, M.M., Brown, P.O. et al. (2002) Identification of genes periodically expressed in the human cell cycle and their expression in tumors *Mol. Biol. Cell* **13**, 1977–2000

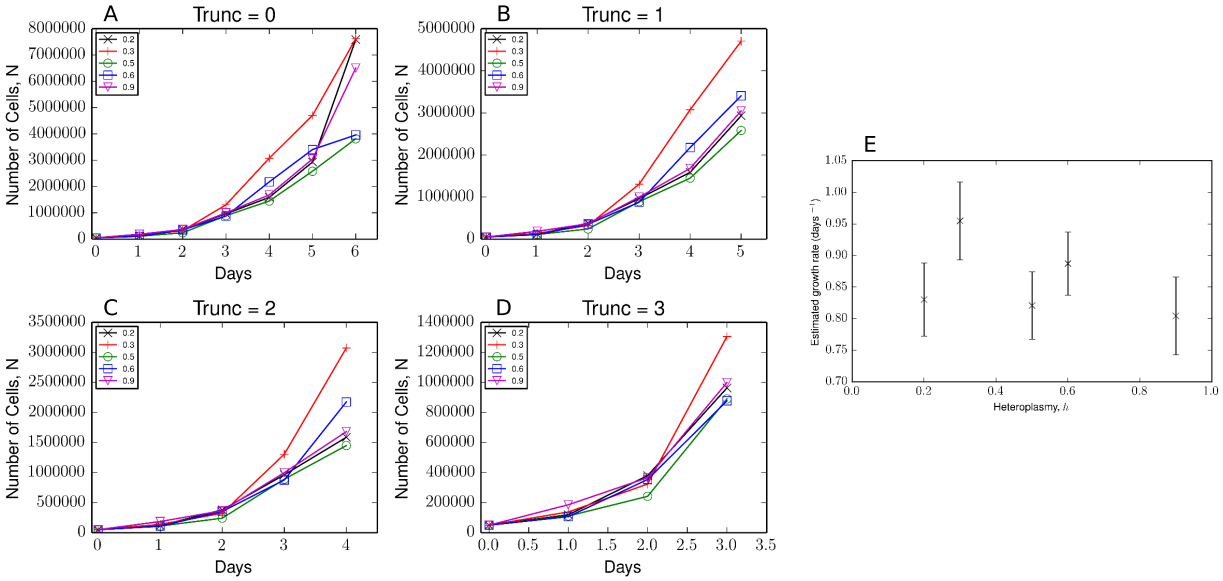

Figure S1. Cell proliferation data from [13]. A-D. Number of cells (N) versus number of days of incubation, for different heteroplasmies, where a number of data points have been truncated (Trunc) from the right. Growth appears to be non-exponential by day 6, and is therefore removed subsequently. E. Slope of linear regression with associated standard error, to derive the growth rate in dimensions of days^{-1}, as used in Fig. 1E. Raw data provided by Martin Picard.

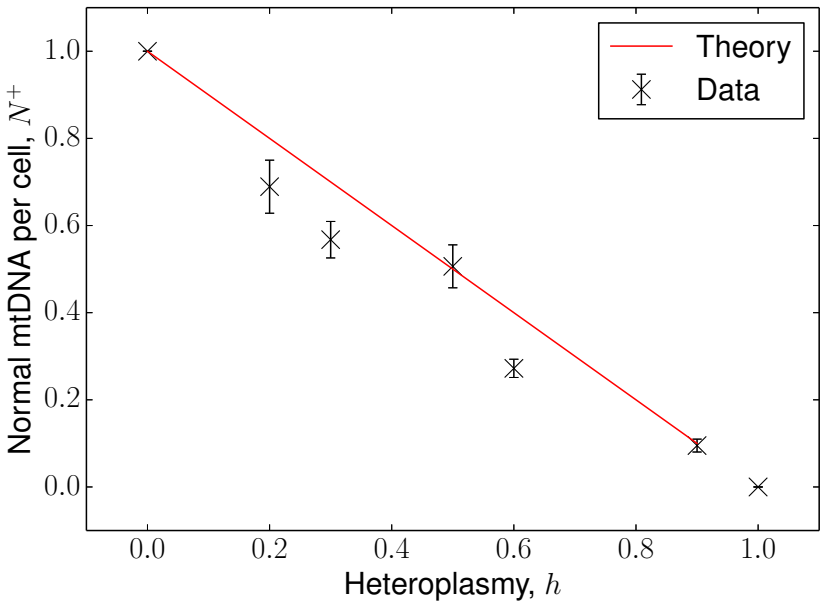

Figure S2. Model fit for wild-type mtDNA copy number Data for mtDNA copy number from Picard *et al.* [13] was multiplied by (1-h), as was the SEM. Displaying the model $N^+ = N(1-h)$, for $N = \text{const} = 1$.

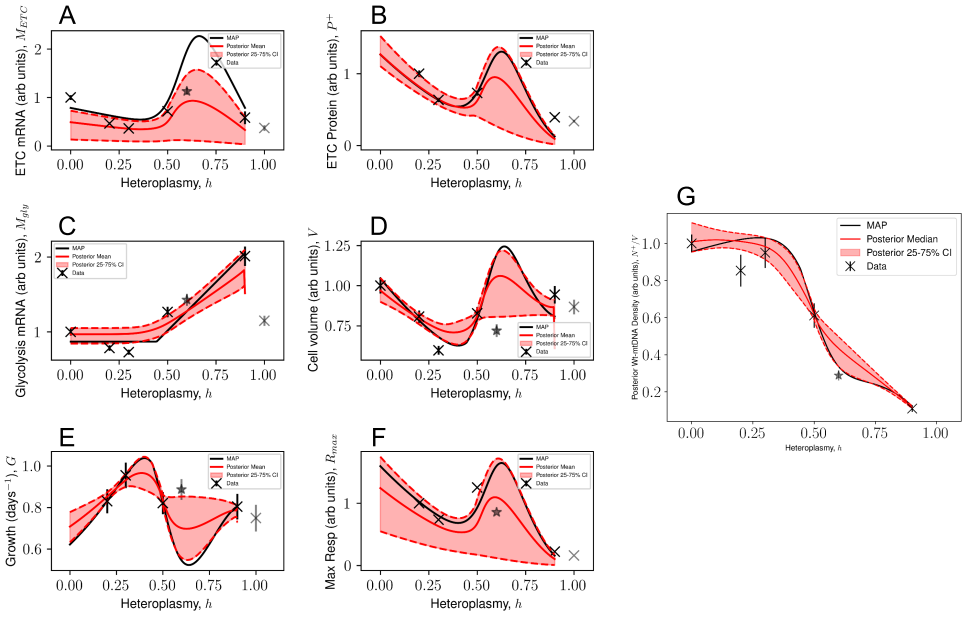

Figure S3. Model fits are largely robust to exclusion of data at 60% heteroplasmy. All data, if present, for $h = 0.6$ (grey stars) were excluded and the model was re-fitted as per Text S2. (A-F) We observe the same qualitative behaviour as Fig. 3. M_{ETC} fits are expected to display a peak around $h = 0.6$ (see posterior mean), as is P^+. M_{gly} is essentially unaffected, whereas V, G and R_{max} also show exaggerated behaviour relative to Fig. 3 at $h = 0.6$. (G) The mean posterior density of N^+/V is approximately constant between $0 \leq h \leq 0.3$, as seen in Fig. 4, suggesting that the hypothesis of wild-type density homeostasis is robust under the exclusion of this data point, given our model structure and priors.

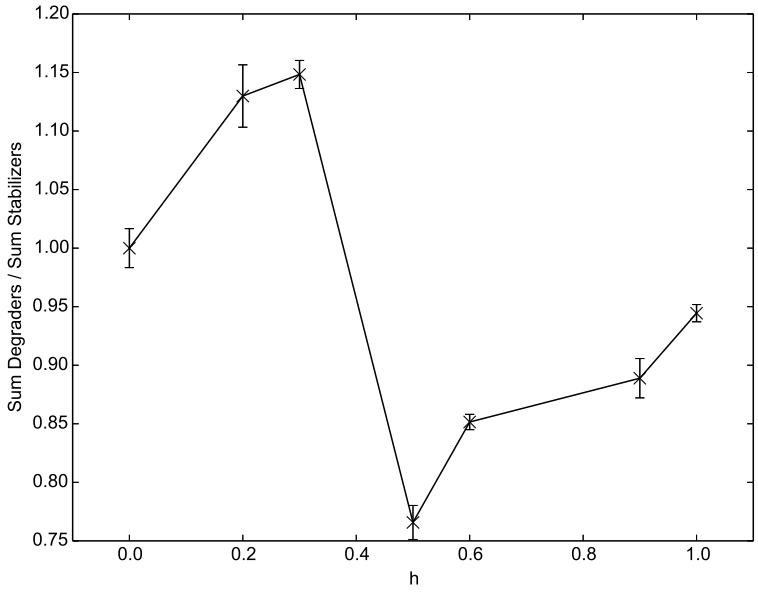

Figure S4. Corroborating evidence for ETC mRNA degradation from Picard *et al*. Ratio of mitochondrial mRNA degraders (PDE12, PNPT1, SUPV3L1) to stabilizers (MTPAP, LRPPRC, SLIRP), see Ref. [28] and references therein. We observe qualitative similarity in δ_m (see Fig. 5) and the ratio of normalised genes, both showing strong downregulation between $h = 0.3$ and $h = 0.5$. The numerator and denominator were normalised according to Eq.(1). Errors result from error propagation of a ratio, where the error for the numerator and denominator are derived using Eq.(2).

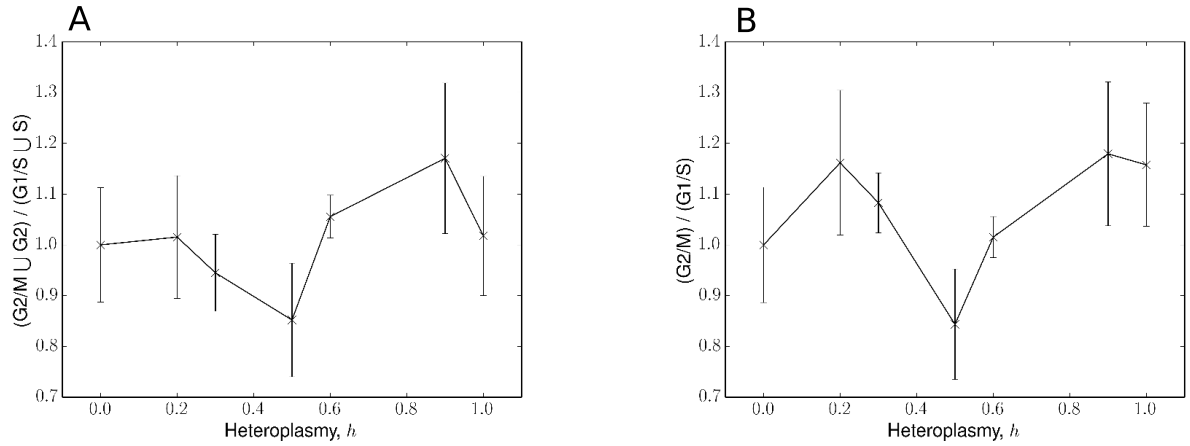

Figure S5. Variation of cell cycle markers with heteroplasmy A list of cell cycle markers, taken from [45] were normalised according to Eq.(1), yielding gene lists for G1/S, S, G2 and G2/M phases. A. The ratio of G2/M to G1/S genes yielded no obvious trend with heteroplasmy. B. G2/M and G2 gene lists were combined (G2/M $\bigcup$ G2), as were G1/S and S (G1/S $\bigcup$ S). This again yielded no obvious trend with heteroplasmy. Errors result from error propagation of a ratio, where the error for the numerator and denominator are derived using Eq.(2).

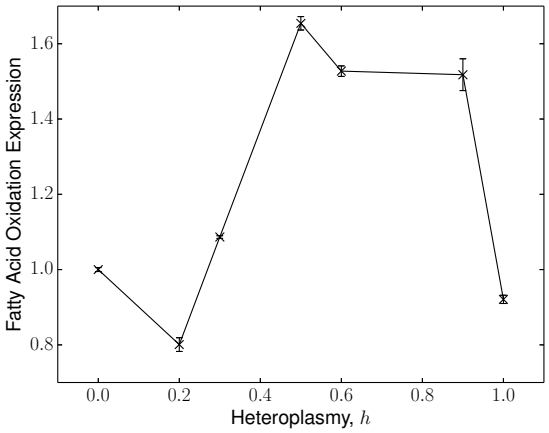

Figure S6. Expression of fatty acid oxidation enzymes with heteroplasmy. Showing variation of the genes (ACADVL, ECHS1, HADH and ACAA2) with heteroplasmy, normalised according to Eq.(1). It can be seen that these metabolites are downregulated between $h = 0.9 \rightarrow 1$, so fatty acid oxidation does not appear to be supporting the maintained cell volume and growth rates over this range of heteroplasmy. Errors are calculated using Eq.(2).

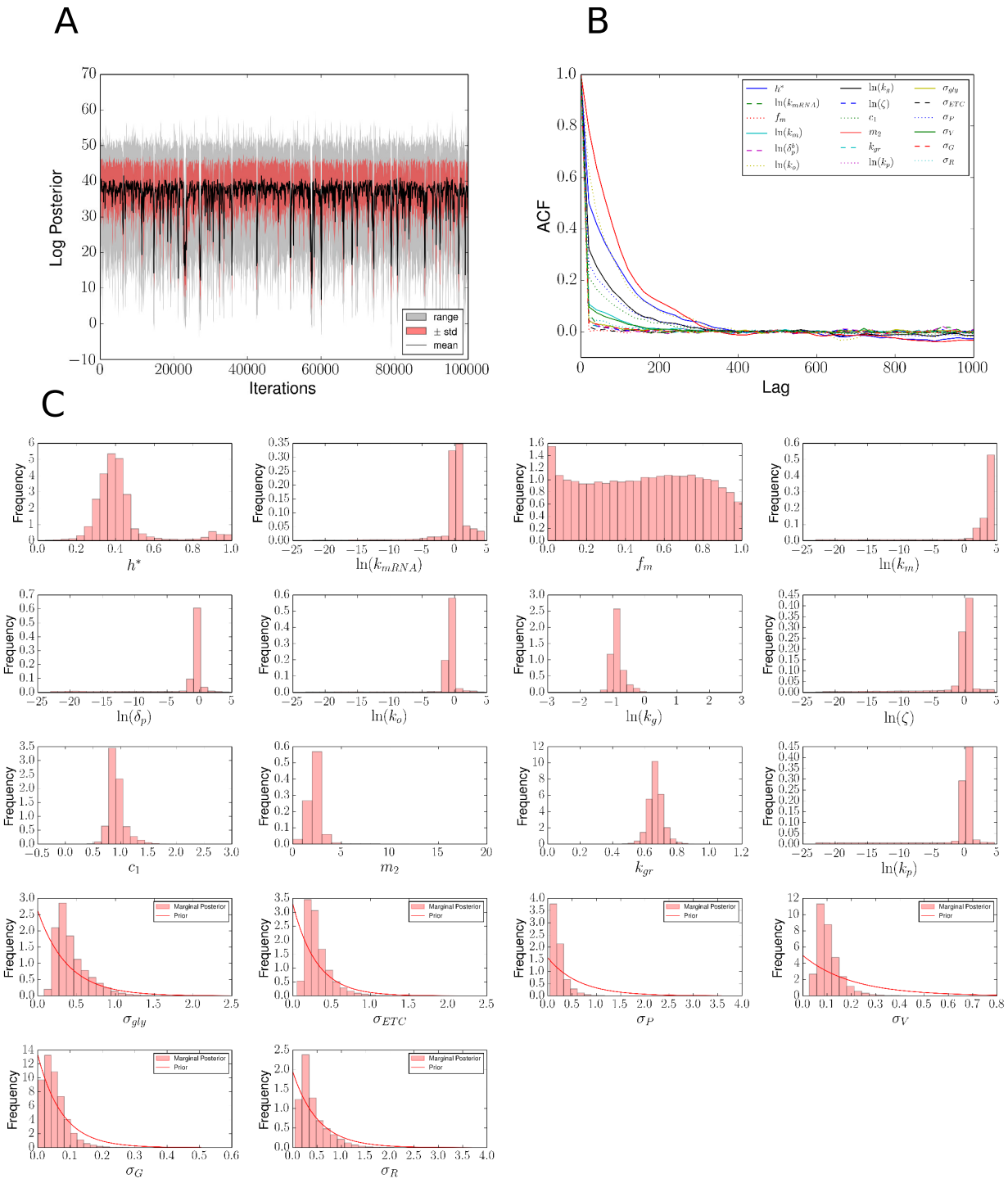

Figure S7. Metropolis-Hastings posterior samples for main model 10^{10} iterations of Metropolis-Hastings were performed, which were thinned to 10^5 samples. The hyperparameter for model uncertainty, Ω, was chosen as $\Omega = 2$ (see Text S2). A. Trajectory of the unnormalised log posterior after thinning. Samples are split into bins of 100 iterations; displaying mean, standard deviation and range of each bin. B. Autocorrelation function for each parameter, on thinned samples. C. Approximate marginal posterior distributions for each parameter in the model. Exponential priors for model uncertainties are plotted, all other priors are uniform (see Text S2).

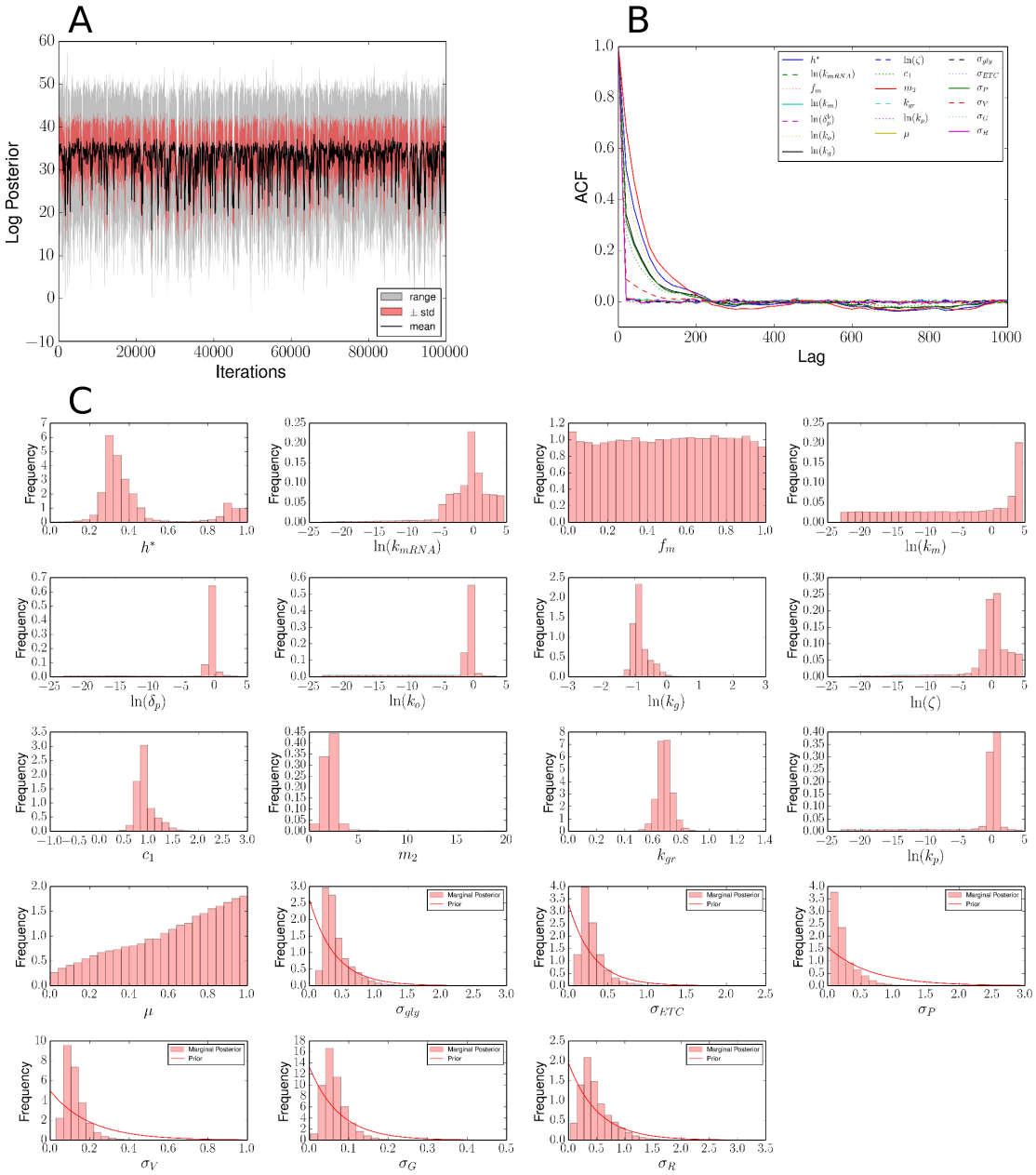

Figure S8. Metropolis-Hastings posterior samples for mutant transcription model 10^{10} iterations of Metropolis-Hastings were performed, which were thinned to 10^5 samples. The hyperparameter for model uncertainty, Ω, was chosen as $\Omega = 2$ (see Text S2). The prior for the additional parameter μ was chosen to be a uniform distribution between 0 and 1. A. Trajectory of the unnormalised log posterior after thinning. Samples are split into bins of 100 iterations; displaying mean, standard deviation and range of each bin. B. Autocorrelation function for each parameter, on thinned samples. C. Approximate marginal posterior distributions for each parameter in the model. Exponential priors for model uncertainties are plotted, all other priors are uniform (see Text S2). Note the marginal distribution of μ peaks near 1.

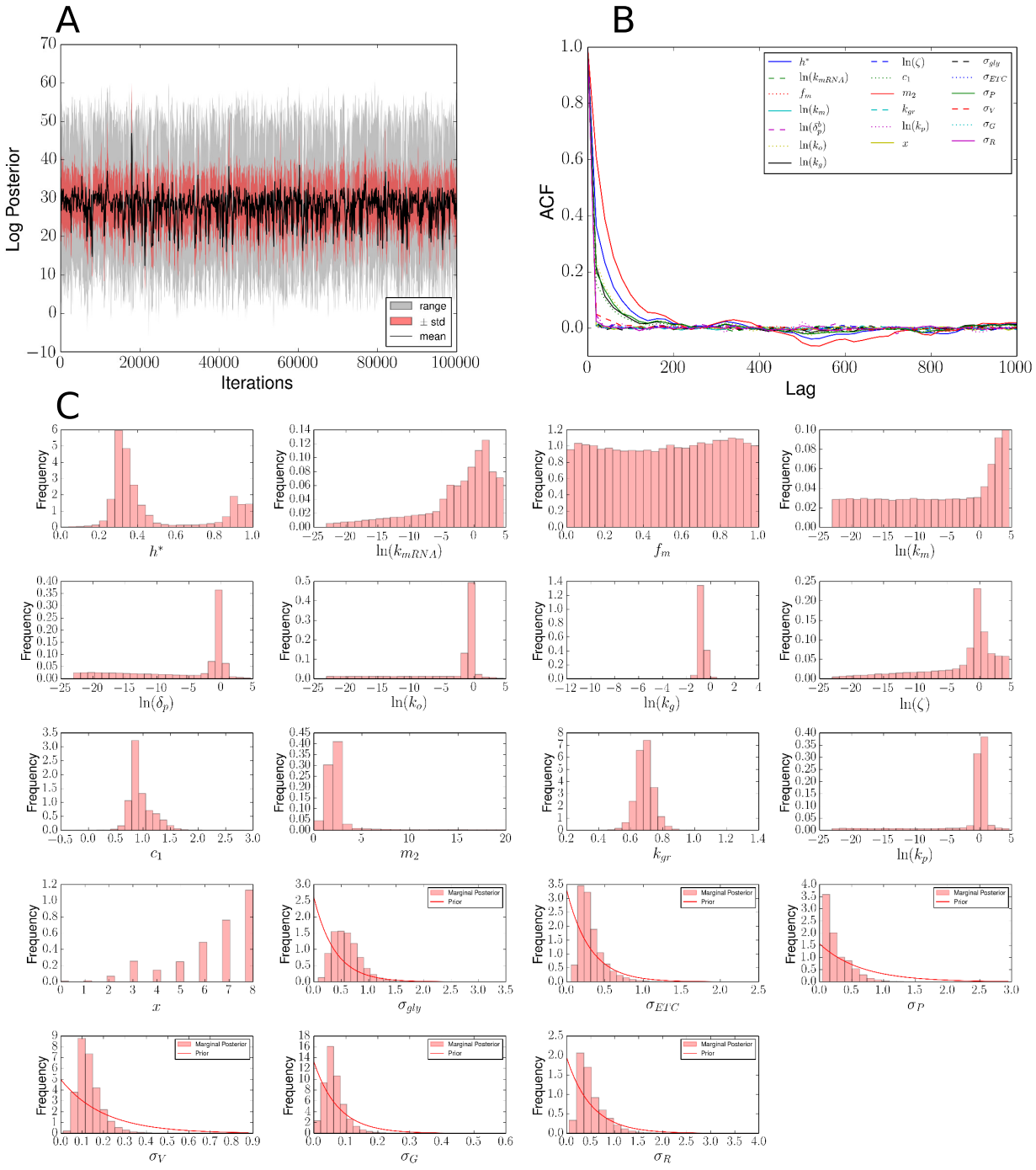

Figure S9. Metropolis-Hastings posterior samples for tRNA misincorporation model 10^{10} iterations of Metropolis-Hastings were performed, which were thinned to 10^5 samples. The hyperparameter for model uncertainty, Ω, was chosen as $\Omega = 2$ (see Text S2). The prior for the additional parameter x was chosen to be a uniform discrete distribution between 0 and 8. A. Trajectory of the unnormalised log posterior after thinning. B. Autocorrelation function for each parameter, on thinned samples. C. Approximate marginal posterior distributions for each parameter in the model. Exponential priors for model uncertainties are plotted, all other priors are uniform (see Text S2). Note the marginal distribution of x peaks at 8, which we expect to be incorrect.

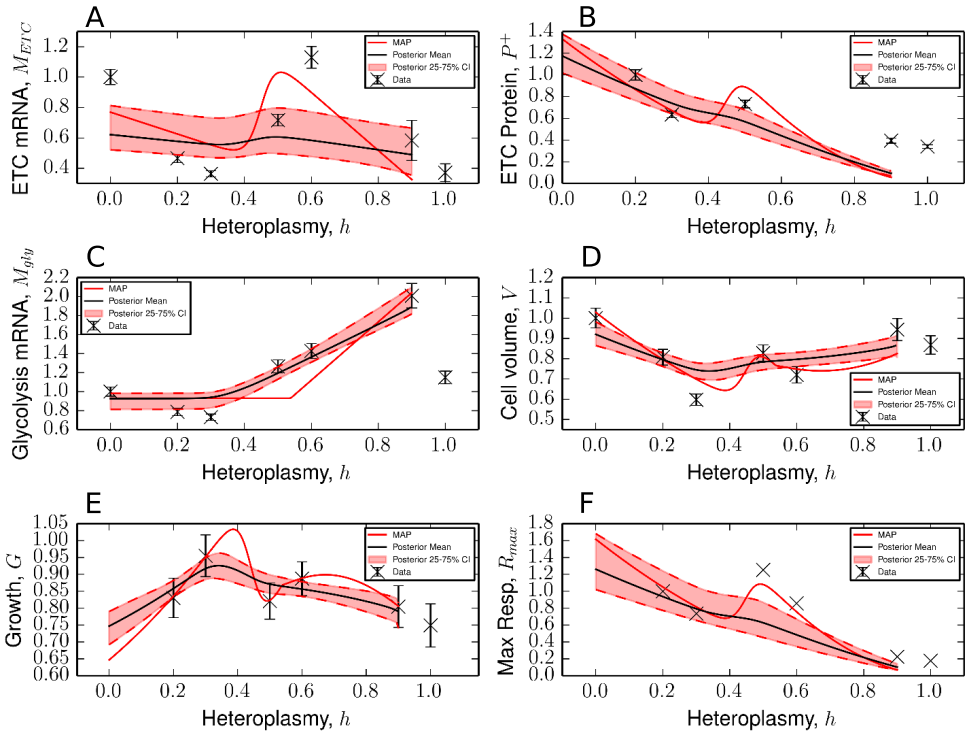

Figure S10. Alternative mutant transcription model. A-F. Model fit when Eq.(5) is replaced with Eq.(S34). The 25-75% CI is flatter when compared with Fig. 3. We find this is due to the model more frequently selecting linear fits to the data, see Figure S16.

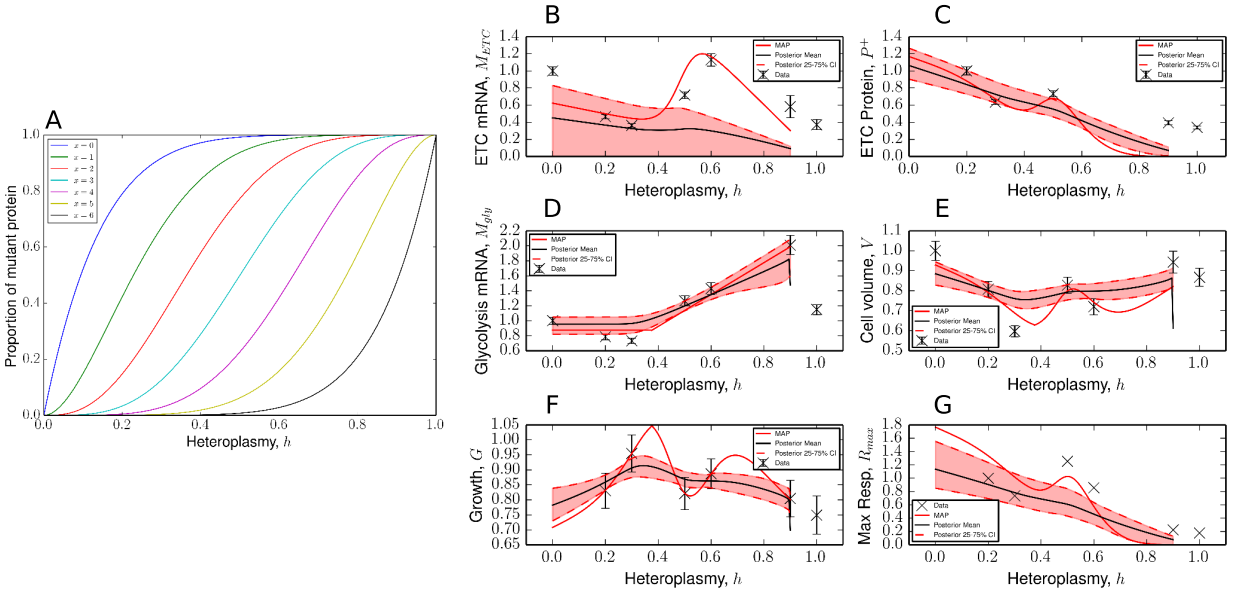

Figure S11. Alternative tRNA misincorporation model A. Expected proportion of mutant protein due to the MELAS mutation, given that each protein can tolerate x mutated residues. The chain length used is $N = 8$, which is the mean number of susceptible residues across all mitochondrially-encoded peptides, excluding ATP8 and ATP6 [9]. B-G. Model fit when Eq.(7) is replaced with Eq.(S37). M_{ETC} is qualitatively fitted more poorly than Fig. 3 (see also Figure S16), although the maximum a posteriori estimate is a closer fit, when compared with Fig. 3.

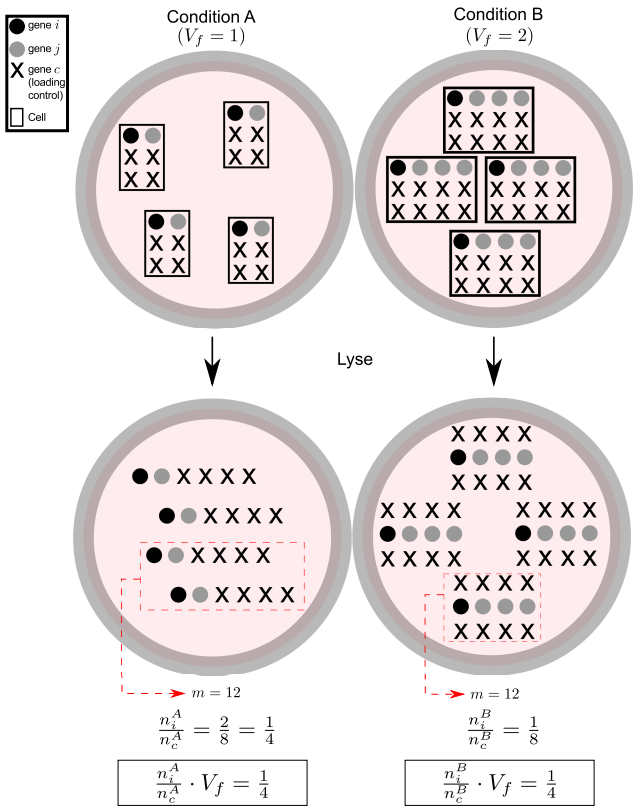

Figure S12. Transformation of Western blot (or RNA-seq) data to per-cell dimensions. Consider a Western blot experiment, where we are interested in the fold-change expression of gene i per cell (n_i), and cell volume has a fold change $V_f = 2$ between conditions A and B. In this example, $n_i^A = n_i^B$. Taking an unbiased sample of size $m = 12$ from each condition, and dividing by the loading control, yields a quantity $1/V_f$ too small. It is necessary to multiply the ratio by V_f, to get an accurate measurement of gene i, in the context of strongly varying cell volume, as is the case in Picard *et al.* [13]. A similar argument holds for RNA-seq data, which also uses a fixed mass of RNA as the starting sample.

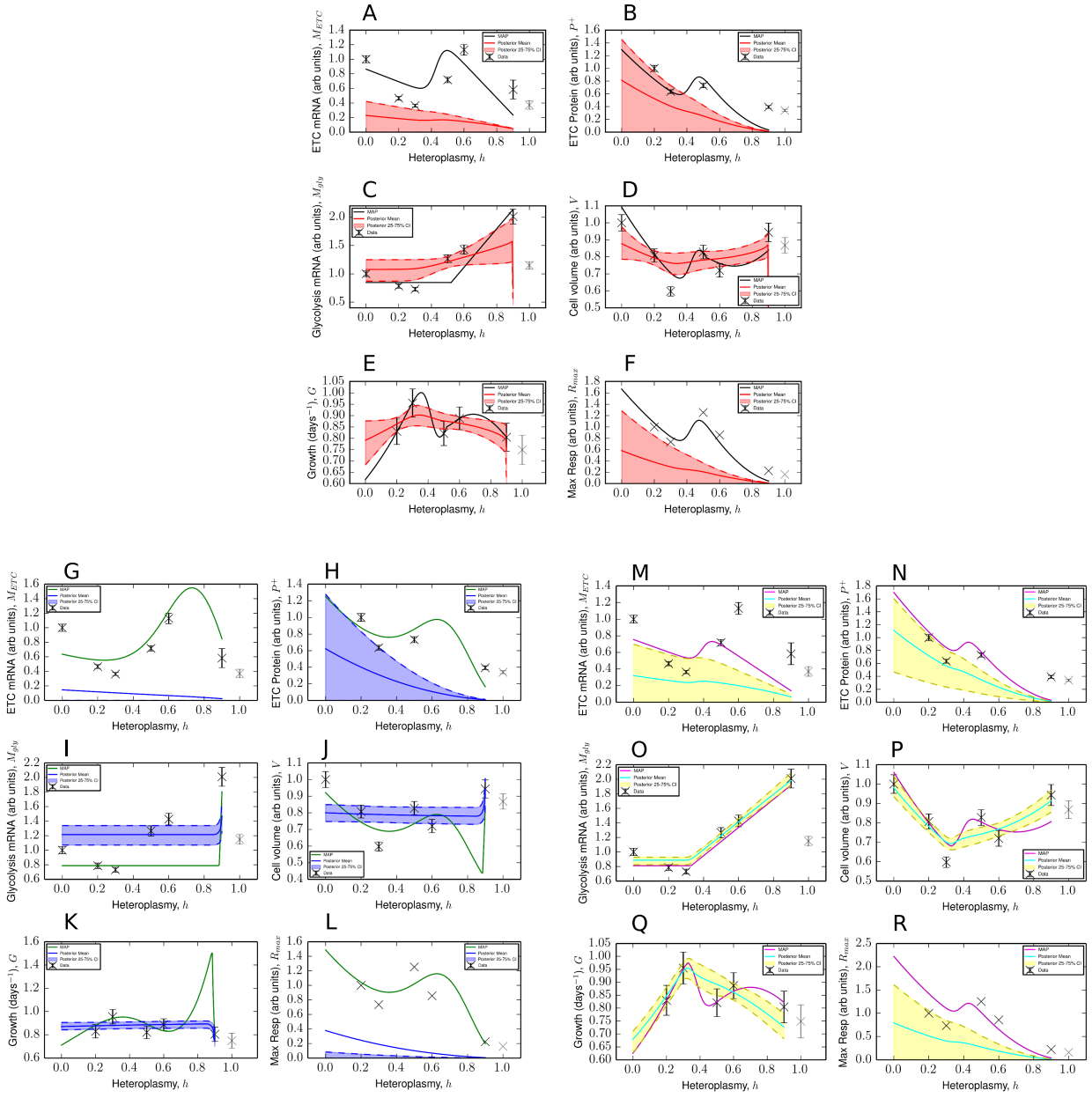

Figure S13. Hyperparameter choice for error model A-F: Model support for when $\Omega = 0$, corresponding to an improper uniform prior on the variance of each feature. G-L: Sub-samples of posterior where $0.85 \leq h^* \leq 0.9$. M-R: Sub-samples of posterior where $0.3 \leq h^* \leq 0.35$. We see a physiologically implausible fit for $0.85 \leq h^* \leq 0.9$, whereas when $0.3 \leq h^* \leq 0.35$ model fits were better able to describe the data (for instance, by comparing G to M).

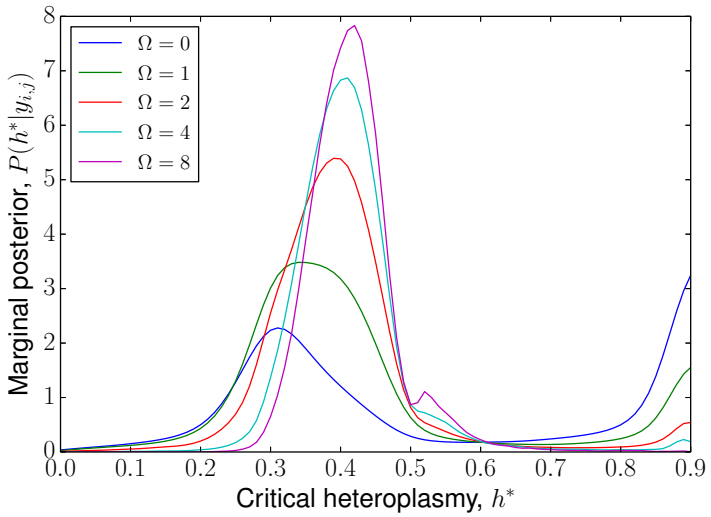

Figure S14. Choice of uncertainty prior affects distribution of critical heteroplasmy and model fit Larger values of Ω suppresses large values of model uncertainty (σ_i, see Eq.(S10)), and consequently forces the model fit to more closely match the data. This corresponds to the h^* mode approximately between 0.3-0.4 see Figure S13.

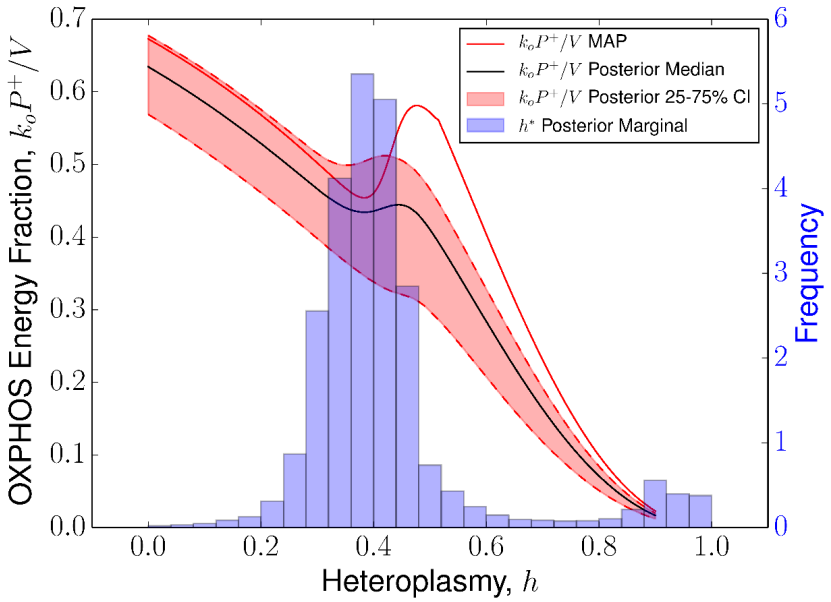

Figure S15. Relative contribution of OXPHOS to total power supply across heteroplasmy Posterior statistics for the ratio of OXPHOS power supply (k_oP^+) to total power supply $k_oP^+ + k_gM_{\text{gly}} = V$. The contribution of ETC power production reduces until the critical heteroplasmy h^*, where a compensatory response stabilizes OXPHOS contributions. As $\delta_m \to 0$ at $h \approx 0.5$ (see Fig. 5), OXPHOS power contributions continue to diminish.

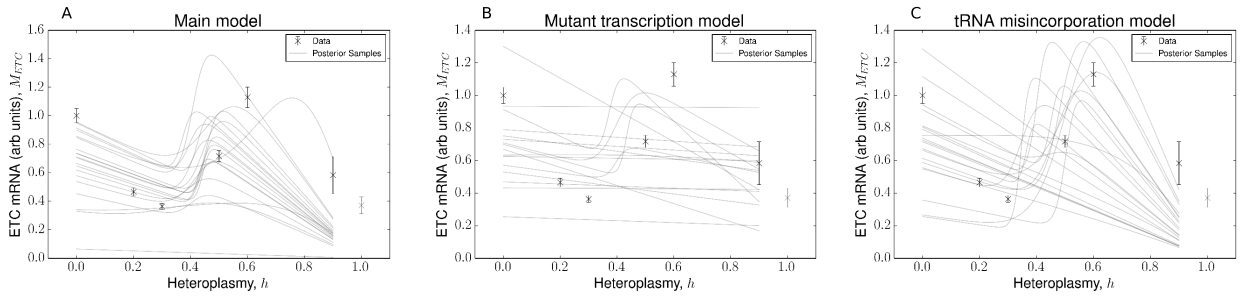

Figure S16. Comparison of ETC mRNA levels for alternative models. Sample of 20 randomly sampled trajectories from the posterior distribution of M_{ETC} for A. Main model (see Interactions between Bioenergetic Variables can be Cast as a Bottom-up Quantitative Model); B. Mutant transcription model (see Text S5); C. tRNA misincorporation model (see Text S5). In models (B) and (C), we find that linear fits are more frequently selected when compared to our main model (A), despite being more complex in terms of number of parameters.

Table S1. Table of observables, and their corresponding parameters

Observables	**Parameter**	**Description**
M_{ETC} and M_{gly}	h^*	Critical heteroplasmy
M_{ETC}	k_{mRNA}	Maximum ETC mRNA degradation rate
	f_m	Relative ETC mRNA degradation rate at h^*
	k_m	ETC mRNA degradation steepness
	ζ	β/k_{mRNA} where β = ETC mRNA transcription rate
P^+	δ_p	ETC protein passive degradation rate
M_{gly}	c_1	Glycolysis mRNA pool size for $h \leq h^*$
	m_2	Glycolysis rate of increase with h, for $h > h^*$
V	k_o	ETC protein constant of proportionality
	k_g	Glycolysis mRNA constant of proportionality
G	k_{gr}	Constant of proportionality
R_{max}	k_p	Constant of proportionality

Table S2. Summary of experimental proposals, corresponding to the claims of the model.

Claim	**Experiment**
MtDNA copy number affects volume	Perturb mtDNA copy number (ddC or PGC1-α), measure volume
Wild-type mtDNA density affects h^* (bioenergetic)	Increase nDNA content, perform RNA-seq
Wild-type mtDNA density affects h^* (mechanical)	Reduce cell volume, perform RNA-seq
Mutant mtDNAs have transcription defect	Measure normal/mutant tRNA abundance with RT-qPCR
Mitochondrial tRNAs have low diffusivity	Fluorescent labelling of mtDNA and tRNA or mRNA encoding tRNA
Cell cycle variation with heteroplasmy	Fucci markers in heteroplasmic cells
Mean cell volume affects growth rate	Synchronise, sort by volume, and measure growth rate
Maximum respiratory capacity $\propto$ ETC protein	Measure $R_{\max}$ at $h = 0$ and P^+ at $h = 0.0, 0.6$